JGR Planets

RESEARCH ARTICLE
10.1029/2024JE008479

Key Points:
- The Martian tropical cloud belt exhibits eastern—western zonal oscillations that are most prominent in late northern summer
- Tropical Cloud Oscillations are controlled by large-scale low frequency equatorial Kelvin and Rossby waves
- Equatorial wave dynamics may have an important effect on the Martian water and dust cycles

Supporting Information:
Supporting Information may be found in the online version of this article.

Correspondence to:
H. Wang,
hwang@cfa.harvard.edu

Citation:
Wang, H., Richardson, M. I., Toigo, A. D., & Newman, C. E. (2024). Large scale oscillations in the Martian tropical cloud belt. *Journal of Geophysical Research: Planets*, *129*, e2024JE008479. https://doi.org/10.1029/2024JE008479

Received 3 MAY 2024
Accepted 30 SEP 2024

Author Contributions:
Conceptualization: Huiqun Wang, Mark I. Richardson, Anthony D. Toigo
Data curation: Huiqun Wang
Formal analysis: Huiqun Wang
Funding acquisition: Huiqun Wang, Mark I. Richardson, Anthony D. Toigo
Investigation: Huiqun Wang, Mark I. Richardson, Anthony D. Toigo
Methodology: Huiqun Wang
Project administration: Huiqun Wang
Resources: Huiqun Wang
Software: Huiqun Wang, Anthony D. Toigo
Supervision: Huiqun Wang
Validation: Huiqun Wang
Visualization: Huiqun Wang, Mark I. Richardson, Anthony D. Toigo
Writing – original draft: Huiqun Wang, Mark I. Richardson
Writing – review & editing: Huiqun Wang, Mark I. Richardson, Anthony D. Toigo, Claire E. Newman

Large Scale Oscillations in the Martian Tropical Cloud Belt

Huiqun Wang[1], Mark I. Richardson[2], Anthony D. Toigo[3], and Claire E. Newman[2]

[1]Center for Astrophysics, Harvard-Smithsonian, Cambridge, MA, USA, [2]Aeolis Research, Chandler, AZ, USA, [3]John Hopkins University Applied Physics Laboratory, Laurel, MD, USA

Abstract The Tropical Cloud Oscillation (TCO) in the Martian atmosphere is a shift of clouds in the northern spring and summer tropical cloud belt between the eastern and western hemispheres on an intra-seasonal timescale of about 10–40 sols. The TCO is a significant intraseasonal variation and may strongly affect the Martian general circulation, water cycle, and dust cycle. We examine TCOs using multiple data sets with a focus on the clouds observed in Mars Daily Global Maps during Mars Year (MY) 29–35. One or more TCO cycles are observed in each MY and the phenomenon is most prominent during $L_s = 135°–185°$. Space-time spectral analysis shows a variety of waves which appear to follow the theoretical dispersion relationships of equatorial waves, such as Kelvin waves, Rossby waves, and Mixed Rossby Gravity waves. The TCO appears to be controlled by zonal wavenumber one traveling waves with Kelvin and Rossby wave characteristics and exhibits a fine-scale latitudinal structure that requires modeling with sufficient resolution. Issues with current data assimilation products for use in studies of Martian equatorial waves due to this fine-scale structure are discussed.

Plain Language Summary During martian northern spring and summer, a relatively thick water ice cloud belt is observed in the tropics (approximately 25°S–25°N), which modifies large-scale circulation, global water transport and the atmospheric dust cycle. We report on a Tropical Cloud Oscillation (TCO) that is a periodic shift in the thickness of this cloud belt between the eastern and western hemispheres on timescales (about 10–40 Mars days) longer than that of weather but shorter than that of seasons. Since the TCO involves changes in clouds and implies changes in circulation, it may also modulate the dust and water cycles. We examine TCOs using image data for Mars Year 29–35 (late 2007 through early 2021). One or more TCO cycles are observed in each Mars Year and the phenomenon is most prominent in late northern summer. A wide variety of atmospheric waves are found during TCOs; however, the most important are equatorial waves traveling eastward and westward with one peak and one trough around the planet. These waves have narrow latitudinal length scales and thus require high resolution numerical models to simulate and properly represent in data assimilation products.

1. Introduction

The Martian tropical cloud belt, composed of water ice clouds, is prominent during northern spring and summer, and is sometimes referred to as the aphelion cloud belt (Clancy et al., 2017; Guha et al., 2021; Wolff et al., 2019a). Its radiative effect can significantly alter atmospheric thermal structure and circulation, though the effect of latent heating is weak and generally negligible (Kahre et al., 2023; Richardson et al., 2002; Steele et al., 2014; Wilson & Guzewich, 2014). The broad seasonal evolution of the cloud belt is conveniently described using the pseudo-season terminology of Wang et al. (2023) which splits a Martian year into six L_s intervals based on distinct behaviors of the dust and water cycles. The tropical cloud belt observed in visible images begins to form during Unober ($L_s = 0°–70°$) when an overturning northern summer Hadley circulation develops in concert with limited water vapor supply from the northern seasonal cap. The cloud belt is in its fully developed state during Duober ($L_s = 70°–135°$) (Smith, 2008; Wolff et al., 2019a), coinciding with the ample supply of water vapor from the exposed northern polar water ice cap and the peak intensity of the northern summer Hadley circulation. The cloud belt dissipates in Triober ($L_s = 135°–185°$) as the major water vapor source is cut off and the northern summer Hadley circulation diminishes (Kahre et al., 2023; Richardson et al., 2002). Note that while the L_S intervals for the pseudo-seasons are uneven in length, they are motivated by observed sharp transitions in seasonal climatic behavior (Wang, Saidel, et al., 2023).

While the seasonal and diurnal evolutions of the tropical cloud belt have been documented extensively (e.g., Giuranna et al., 2021; Smith, 2019; Wolff et al., 2022), the intra-seasonal variability of the cloud belt has only recently been recognized (Wang & Gonzalez Abad, 2021). The reason is in part due to the need for a long record

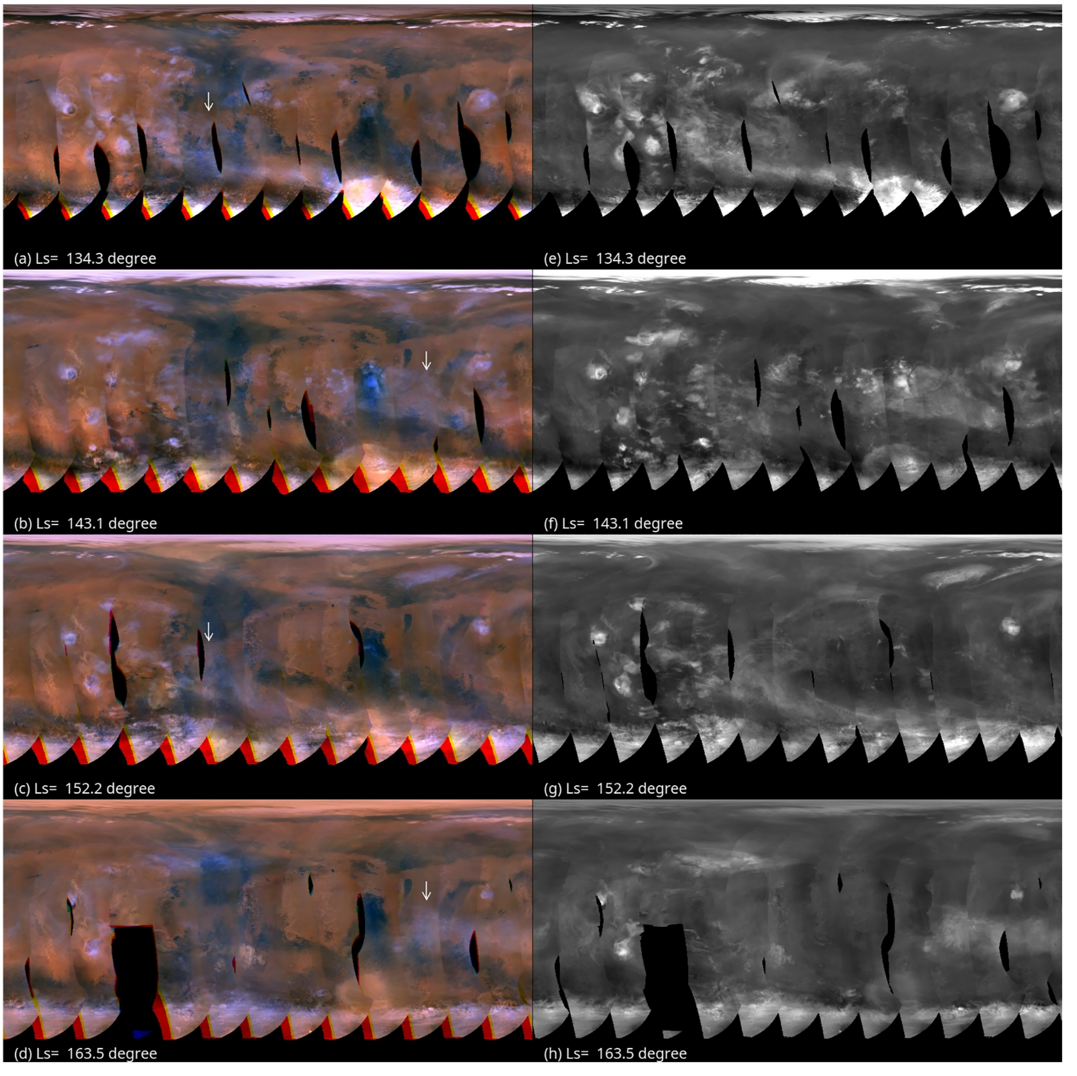

Figure 1. Color (left column) and blue (right column) Mars Daily Global Maps for Mars Year 30 (a, e) L_s = 134.3°, (b, f) L_s = 143.1°, (c, g) L_s = 152.2°, and (d, h) L_s = 163.5°. White arrows indicate tropical clouds.

of observations to extract the signature with confidence. While data indicative of the intraseasonal variation existed for the Mars Global Surveyor (MGS) mission (Wang & Ingersoll, 2002), the identification of the signal would have been less conclusive; thus, it was largely neglected in previous studies.

The "Tropical Cloud Oscillation" (TCO) (Wang & Gonzalez Abad, 2021) refers to a shift of cloud activity between the eastern and western hemispheres in the Martian tropics on an intra-seasonal timescale (about 10–40 sols). As an example, Figure 1 shows a TCO cycle for Mars Year (MY) 30 using Mars Daily Global Maps (MDGMs) produced from Mars Reconnaissance Orbiter (MRO) Mars Color Imager (MARCI) images (Wang et al., 2020). The tropical clouds are more extensive in the western hemisphere at L_s = 134°, become more extensive in the eastern hemisphere at L_s = 143°, and so forth, with a quasi-periodicity of about 20 sols. Note that the cloud belt is also experiencing a seasonal decay (dimming) at all longitudes during the process, and thus the TCO does not appear as a simple oscillation.

Study of the TCO can improve the understanding of the interactions among the circulation, dust cycle and water cycle. During northern spring and summer, the cloud belt moderates the cross-equatorial water transport, as the condensation altitude is below the tropical mean top of the Hadley circulation (Kahre et al., 2023; Richardson et al., 2002), which reduces the northern-to-southern transport efficiency (Clancy et al., 1996, 2017). The TCO may modulate this "cold-trap hygropause" as the cloud alternates between one phase of the TCO and the other.

Due to the significant radiative feedback between clouds and circulation, the variations in cloud thickness associated with the TCO could have implications for the dynamics involved in the formation and termination of the cloud belt. Observations suggest a rapid termination of the cloud belt, especially when relatively large dust storms occur (Battalio & Wang, 2019; Willame et al., 2017). Dust perturbations could probably excite waves that can be linked to the TCO, and the mechanisms may plausibly involve the coupling between the dust and water cycles. Finally, the tropical waves associated with the TCO are likely excitable throughout the Martian year and may provide a means of "teleconnection" between regions at great separation. The TCO provides an opportunity to study these waves using visible images and a means of contemplating their roles in a broader sense.

The existence of the TCO is further suggested by the optical depth (τ) data collected by the Mars Exploration Rovers (Lemmon et al., 2004). Both rovers were located near the equator but were separated by about 180° in longitude. The optical depth data show that local peaks are spaced about 15° of L_s (~30 sols) apart in Triober at both locations and that the peaks appear to sometimes alternate between Spirit (175.47°E, 14.57°S) and Opportunity (354.47°E, 1.95°S) (Figure S1 in Supporting Information S1). Interestingly, the TCO may even be related to the decades old telescopic "blue clearing" phenomenon, where observations of surface albedo features (e.g., Syrtis Major) vary between being visible and being obscured by clouds in blue filter images of Mars (Smith, 1961). An intra-seasonal large-scale variation in cloud optical thickness may help explain this occasional clearing of the atmosphere.

In this paper, we investigate tropical cloud variability and its associated constituent tropical waves on intra-seasonal timescales during L_s = 0°–185°. While previous studies of non-tidal traveling waves mainly used thermal data with a focus on extra-tropical waves (Banfield et al., 2004; Barnes et al., 2017; Hinson & Wilson, 2023), this study instead examines large-scale traveling waves in the tropics mainly using imaging data, with a couple of supplementary data sets. Note that this paper loosely refers to 25°S–25°N as the Martian tropics by analogy with the terrestrial definition according to the planet obliquity. However, the exact latitudinal delimiter is inconsequential for this study, as long as the region is not too far from the equator. Section 2 introduces the data sets and methods. Section 3 presents the results. Section 4 provides a summary.

2. Data and Method

This section initially introduces the blue MGDM dataset, which provides optimal information about clouds with high-resolution spatial coverage (Section 2.1). Then, that dataset's relationship with cloud optical depth derived from the MARCI ultraviolet (UV) channel is examined (Section 2.2), and the consistency between the datasets is illustrated (Section 2.3 and 2.4). Finally, the spectral analyses for highlighting the waves in the MDGM data (Section 2.5) and a data assimilation product (Section 2.6) are described.

2.1. Mars Daily Global Maps Exhibiting TCO

This paper takes advantage of the publicly available nearly continuous 0.1° longitude × 0.1° latitude resolution blue-filter MDGMs (180°W–180°E, 90°S–90°N) from MY 29 to 35 (Wang et al., 2020). These MDGMs (Figure 1) were composed using the MARCI wide-angle global map swaths (Bell et al., 2009; Wang & Gonzalez Abad, 2021). Although MDGMs are primarily designed to provide a quick view of the daily Martian weather and to keep a long-term record, they can also be used to study the intra-seasonal behavior of the tropical cloud belt amongst other phenomena (Wang & Gonzalez Abad, 2021; Wang, Saidel, et al., 2023).

The data used for this analysis are the blue-filter component of the MDGMs before they are scaled to the 0–255 data number range and then used in the production of the corresponding color MDGMs (right column of Figure 1, i.e., the mosaics created from the photometrically corrected blue-filter images which are unitless (Wang & Gonzalez Abad, 2021)). We use the blue maps as they have better spatial coverage (fewer gaps) than the 2 UV channel maps and they provide the best indication of water ice clouds amongst the 5 visible channel maps. The pixel values used in this paper are the ratios between the observed blue signals and the modeled values used for photometric correction (Wang & Gonzalez Abad, 2021). The expectation is that the modeled values represent the average behavior for a typical Martian surface and atmosphere observed and illuminated at various angles and thus the ratio has a mean value close to 1. We use the values from the polar cap free area of the planet (50°S–50°N) to remove the small differences in processing between MARCI subphases, as each subphase was processed separately (Wang & Gonzalez Abad, 2021). The median pixel value of all the blue MDGMs over this area is 0.98 and that of each MARCI subphase (which covers an Earth month) varies between 0.94 and 1.08 with a mean of

10.1029/2024JE008479

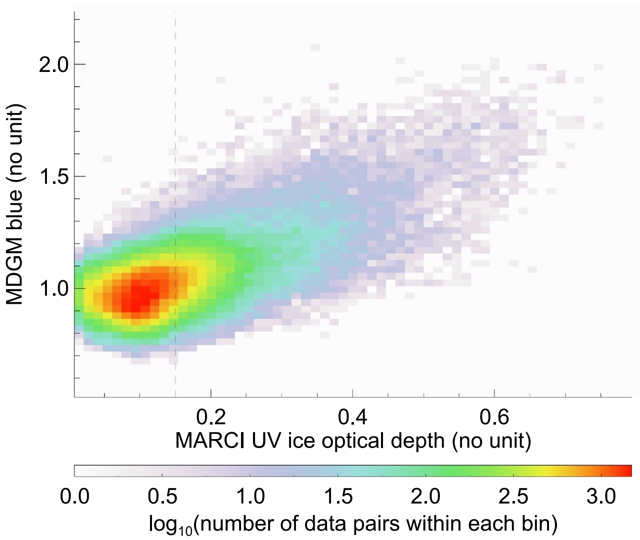

Figure 2. Joint histogram of blue Mars Daily Global Map pixel value versus MARCI UV ice optical depth derived from paired data for Mars Year 33. Colors indicate $\log_{10}$ of the number of data pairs within each bin. The region to the right of the dashed line shows positive correlation.

1.00 ± 0.02. In this study, we apply a scaling factor to all the blue MDGMs in each subphase so that the median of the subphase aligns at 0.98. Deviations from the modeled photometric behavior for any given pixel at any given time will be brighter (>1.0) or darker (<1.0) depending on the scene observed and especially on the presence of surface ice or ice clouds, where the maximum can go substantially above 1 (Figure 2). However, the MDGMs are from afternoon observations, and in the tropics, surface ice does not become an issue for our analysis.

2.2. Blue MDGMs Versus MARCI UV Ice Cloud Retrievals

To illustrate that most of the brightness variation within pre-scaled blue MDGMs is due to water ice clouds, Figure 2 shows the relationship between the blue MDGM pixel values and the water ice cloud optical depths (τ) retrieved from MARCI UV (320 nm) ice cloud optical depth maps by Wolff et al. (2019a). For each valid value in the MARCI UV optical depth map (0.125° longitude × 0.125° latitude) within 5°S–0°S during L_s = 0°–185° of MY 33, we find the blue MDGM pixel value that is closest in space and time. Note that we sampled 5°S–0°S for computational convenience, but the same relationship is obtained if a wider sampling of the tropics is undertaken. The 2D histogram shows $\log_{10}$(count), where count is the number of data pairs in each bin. There is a positive correlation for $\tau > 0.15$ when both data sets are dominated by apparent clouds. For $\tau < 0.15$, weaker or lack of correlation is expected as blue images are more influenced by surface albedo variations when clouds are thinner. Note that the surface albedo is much lower and more uniform in UV than in blue images. Figure 2 also implies that the TCO observed in blue MDGMs is attributable to thicker and/or brighter clouds instead of thinner haze. Fortunately, surface albedo variations in the blue images do not contribute significant power to traveling waves derived from the space-time spectral analysis in subsequent sections.

2.3. Space-Time Evolution in Images

Using the blue MDGMs, we construct longitude versus L_s Hovmöller diagrams (Hovmöller, 1949) for each 0.5° latitudinal band within 20°S–20°N for each MY. The Hovmöller diagram is designed to illustrate the time evolution of coherent spatial structures. An example is shown in Figure 3 for 0.5°S–0°N in MY 33. We have chosen a narrow latitudinal band almost at the equator to illustrate behavior, but the features discussed appear coherent across the tropics (as discussed later). To mitigate the influence of residual image processing artifacts (e.g., seams and opposition surges (Wang & Gonzalez Abad, 2021)) in MDGMs, we used the median pixel value of each 2.5° longitude × 0.5° latitude bin for the construction. Scattered missing data in each diagram (Figure 3a) due to occasional spatial gaps in individual MDGMs are filled in through image inpainting using the OpenCV software library (Bradski, 2000) (although the overall results are insensitive to the gap filling methods). The resulting 2D arrays are then interpolated in time from the MDGM L_s grid to the regular 669-sol MY grid (Figure 3b). The time periods with missing MDGMs spanning >2° L_s are masked out.

For each longitude bin, we remove the seasonal cycle by subtracting a low order polynomial fit (typically order 6) for the corresponding MY. The anomalies (Figure 3c) reflect the brightness variations associated with changes from a couple to a few tens of sols. While most of the signature here is ascribable to water ice clouds, thick dust storms, if they occur, are also noticeable in blue MDGMs. However, large thick dust storms mainly occur in episodes during Quartober (L_s = 185°–245°) and Sextober (L_s = 295°–360°), traveling from the northern to southern hemisphere across the equator (Wang, Saidel, et al., 2023). Thus, they are not particularly active in the seasons covered in this study. Smaller episodes occasionally occur in the southern mid-high latitudes in Triober, but they seldom reach the equator (Wang & Gonzalez Abad, 2021; Wang, Saidel, et al., 2023). Sporadic dust storms will appear like noise in Hovmöller diagrams and are not expected to affect subsequent analysis.

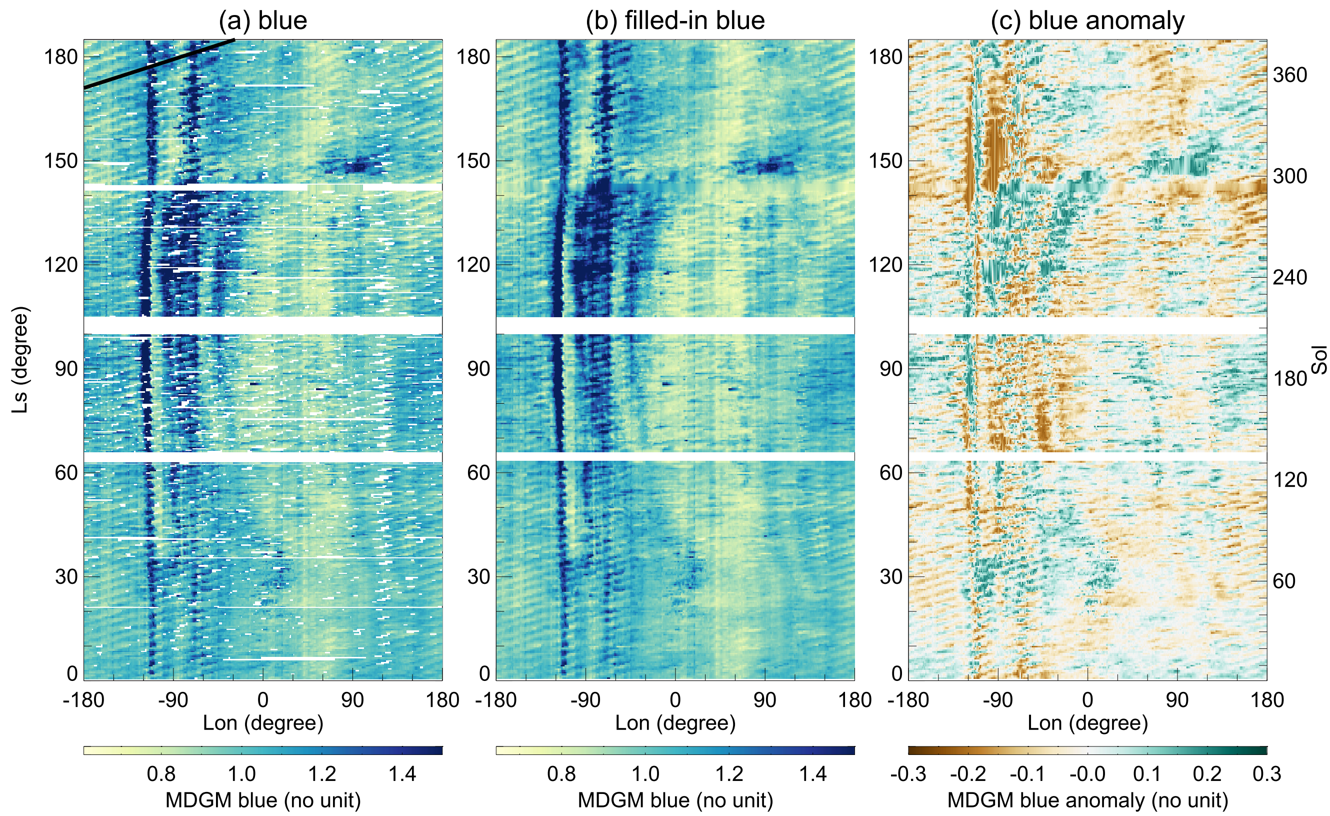

Figure 3. Longitude versus L_s Hovmöller diagrams composed using unitless blue Mars Daily Global Map pixel values within 0.5°S–0.0°S during $L_s = 0°–185°$ of Mars Year 33. (a) The original signal, (b) Same as (a) but with the missing data filled in, (c) Anomaly after seasonal cycle removal from (b). L_s is shown on the left axis. Sol number is shown on the right axis of Panel (c). Time increases upward. The black line in the upper left corner of Panel (a) indicates the presence of the artificial zonal wavenumber $k = 12$, wave period $P = 5$-sol wave due to the Mars Reconnaissance Orbiter spacecraft orbit.

2.4. Space-Time Evolution in Ice Optical Depths

Figure 2 demonstrates in a statistical sense that pixel brightness variations in blue MGDMs indicate the presence of apparent ice clouds. Here, we examine the space and time evolution in MARCI UV ice optical depths (Wolff et al., 2019a) and compare it with Figure 3. We use the same method (Section 2.3) to compose a Hovmöller diagram for 0.5°S–0°N in MY 33 from the cloud optical depths (Figure 4). As the optical depth retrieval is for emergence (i.e., emission) angles $e < 75°$ which cover only the middle portion of each MARCI swath, the gridded data for each sol have large gaps at the low latitudes (see Figure 10 of Wolff et al. (2019a)). The gaps shift longitudinally with the spacecraft orbit pattern; consequently, there are many missing values which show up as sloped white data gaps in Figure 4a. Unlike the UV retrievals, MDGMs attempt to flatten geometry-related brightness variation across each MARCI swath up to $e \sim 89°$ using an empirical correction approach, and this is done so that the left side of a swath can be merged to the right side of the next swath. Wolff et al. (2019a) have noticed substantial variation of tropical clouds even over a single hour of local time (14h30–15h30) covered by MARCI. Thus, the presence of some artifacts at the seams in MDGMs is due to the variation of clouds with local time.

Despite the brightnesses in blue MDGMs not being equivalent to true cloud retrievals and concerns regarding high emergence angles, Figures 3c and 4c show an overall agreement in the patterns of the signals between the MARCI MDGMs and UV ice optical depths. For example, both figures show strong positive and negative anomalies during Ls = 120°–160° which relate to the TCO, and both show a seasonal change near 110°W which relates to the positional shift of Pavonis Mons clouds (Benson et al., 2003). Hence, the tropical anomalies seen in the MDGMs are primarily due to water ice clouds. The UV optical depths more accurately quantify cloud thickness, whereas the MDGMs have fewer gaps and can be used in this study without requiring a retrieval process.

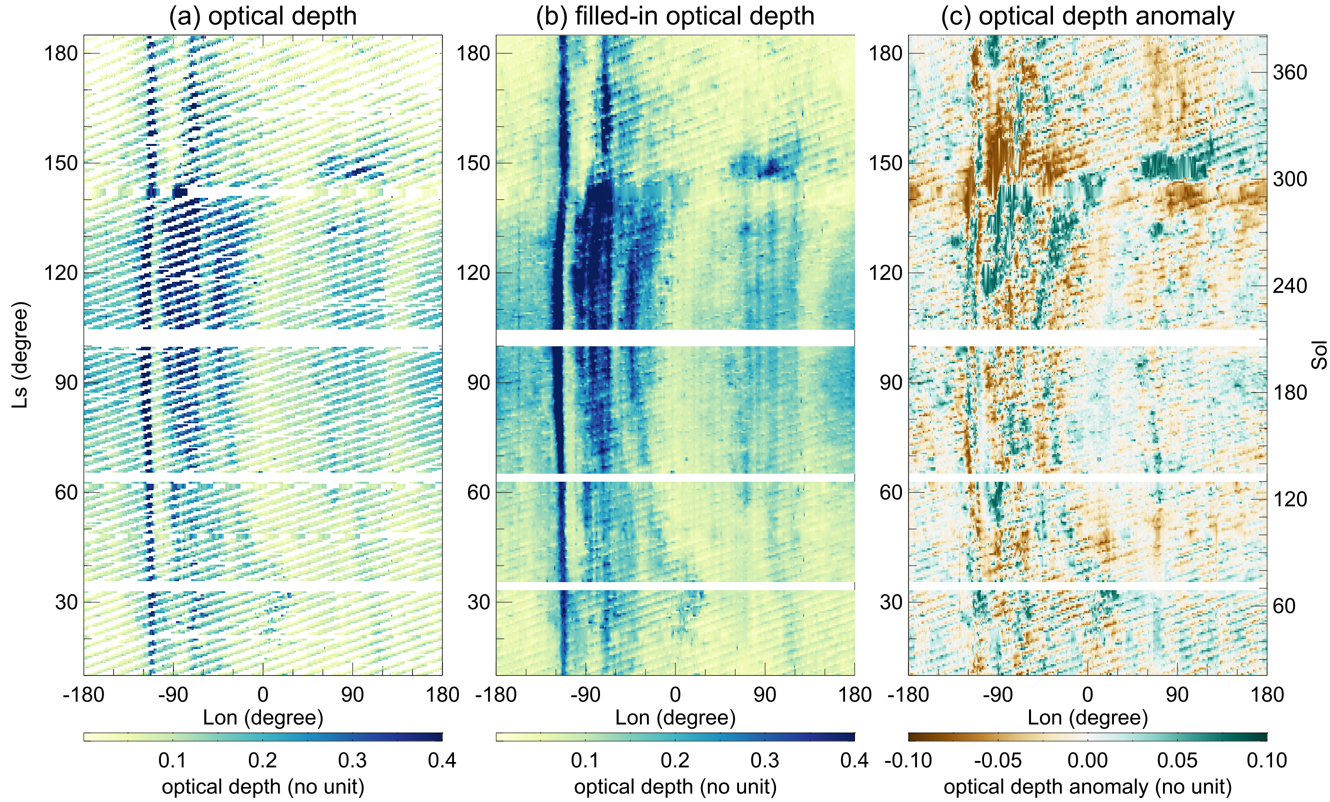

Figure 4. Same as Figure 3 but for the MARCI UV ice optical depth (unitless) of Mars Year 33.

Figures 3 and 4 show a highly regular, fine-scale wave pattern with a zonal wavenumber of $k \sim 12$ and a wave period (P) of ∼5 sols, which is indicated in Figure 3a by a black line (upper left). This pattern stems from the convolution of the strong diurnal cycle of Martian clouds with the ∼5-day repeat cycle of the 12–13 orbits/day MRO orbits (Benson et al., 2003; Wang & Gonzalez Abad, 2021; Wolff et al., 2019a; Zurek & Smrekar, 2007) and is ignored in this study.

2.5. Space–Time Spectra From MDGMs

We derive space-time (zonal wavenumber k vs. time frequency $\omega = 1/P$) wave spectra from the Hovmöller diagrams of the blue MDGM anomalies to investigate the waves during the TCO. Following a common practice (Knippertz et al., 2022; Wheeler & Kiladis, 1998), two-dimensional fast-Fourier transforms (2D FFT) are performed for each 0.5° latitude bin on each of the 144 longitude bins (with 2.5°/bin) × 96 sol segments that stride forward in time every 4 sols. The segment duration is chosen to capture several cycles of the intra-seasonal waves of interest. Before the FFT analysis, the data within each segment are first de-trended and then tapered (using a Hanning window) for each longitude bin. Experiments with 84-sol and 128-sol segments give similar results; thus, this study uses 96-sol for all the analyses.

As an example, Figure 5a shows the k-ω $\log_{10}$ power spectrum derived from the segment corresponding to 0.5°S–0°S and MY 30 $L_s = 125.8°–176.0°$. The plot follows the convention that eastward traveling waves have positive k, westward waves have negative k, and frequencies are positive. As is the case for the terrestrial atmosphere (e.g., Kiladis et al., 2009), the spectrum shows a general tendency for smaller k and ω to have larger power (i.e., red spectrum). In addition, there is a strong peak near $k = 12$, $\omega = 0.2$ cycle/sol ($P = 5.0$ sol), which is an artifact related to the MRO orbit (Section 2.4).

We calculate a mean spectrum by averaging the spectra of all latitude bins within 20°S–20°N, for all Unober-to-Triober segments, and in all Mars years. We also calculate the standard deviation σ at each k- ω location. The mean spectrum (Figure 5b) is a much smoother red spectrum with many regularly ordered peaks. As mentioned before, the largest peak near $k = 12$, $\omega = 0.2$ cycle/sol is due to the convolution of the strong local time variation

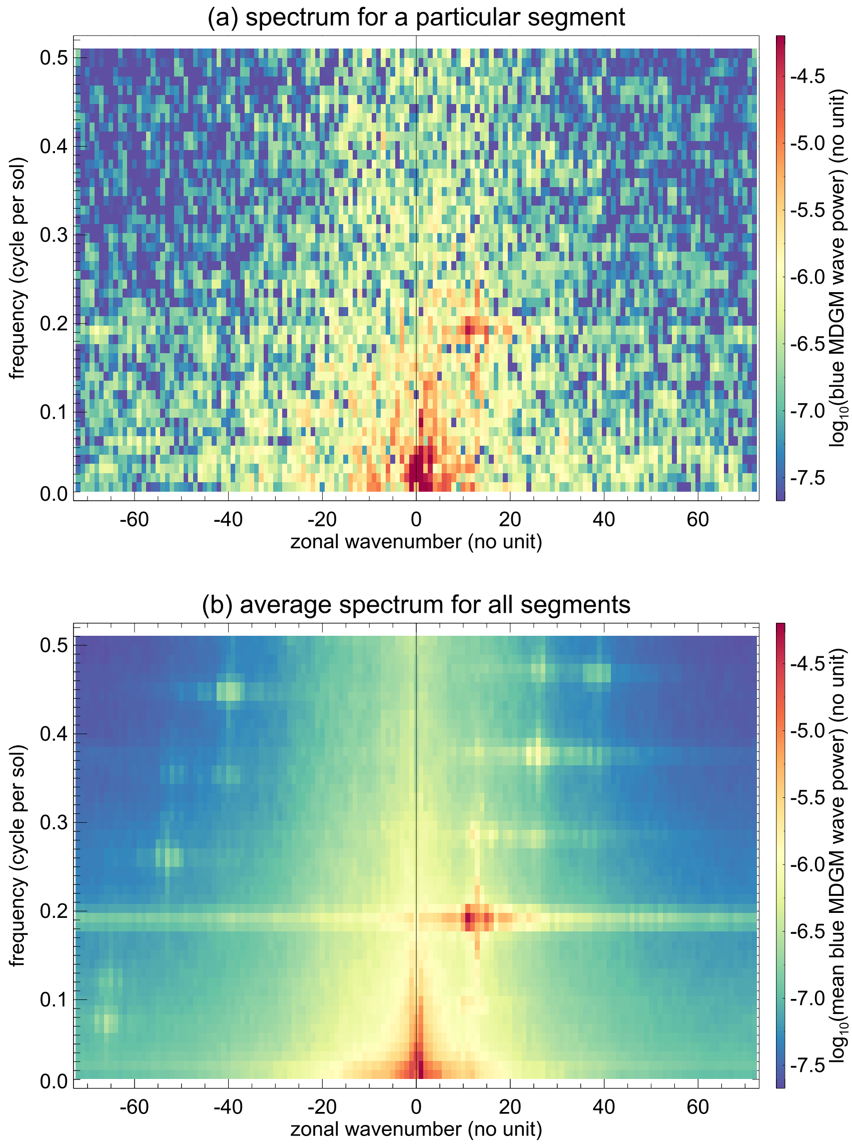

Figure 5. Zonal wavenumber (k) versus time frequency (ω, cycle/sol) spectra derived from the blue Mars Daily Global Maps (MDGMs). (a) $\log_{10}$(blue MDGM wave power) for 0.5°S–0°S and L_s = 125.8°–176.0° of Mars Year (MY) 30, (b) $\log_{10}$(mean blue MDGM wave power) for 20°S–20°N and L_s = 0°–185° of MYs 29–35.

of clouds and the MRO orbit. The artificial peak has many aliases in the k- ω space. As Wu et al. (1995) demonstrated, data observed in a regular pattern will result in such a series of "ghost" peaks, which should be neglected. Indeed, the pattern of "spikes" in Figure 5b closely resembles the "ghost" points associated with spacecraft aliasing as shown in Figure 3 of Wu et al. (1995).

Terrestrial equatorial wave analysis typically identifies different wave types from the mean spectrum by removing a background spectrum which can be a smoothed version of the mean spectrum (Knippertz et al., 2022; Wheeler & Kiladis, 1998). For this study, due to the lack of a priori knowledge of Martian equatorial waves and numerous suspicious "ghost" peaks in the mean spectrum (Figure 5b), we decided to investigate the waves during TCOs by comparing the relevant individual spectra with the mean spectrum. To simplify the analysis, we concentrated on $k < 12$ and manually zeroed out the frequencies likely influenced by "ghost" peaks. These ghost frequencies are identified as obvious local maxima along ω in the mean spectrum (Figure 5b), and they are roughly equally spaced (Figure S2 in Supporting Information S1). For the time periods exhibiting a strong TCO in images, we designate

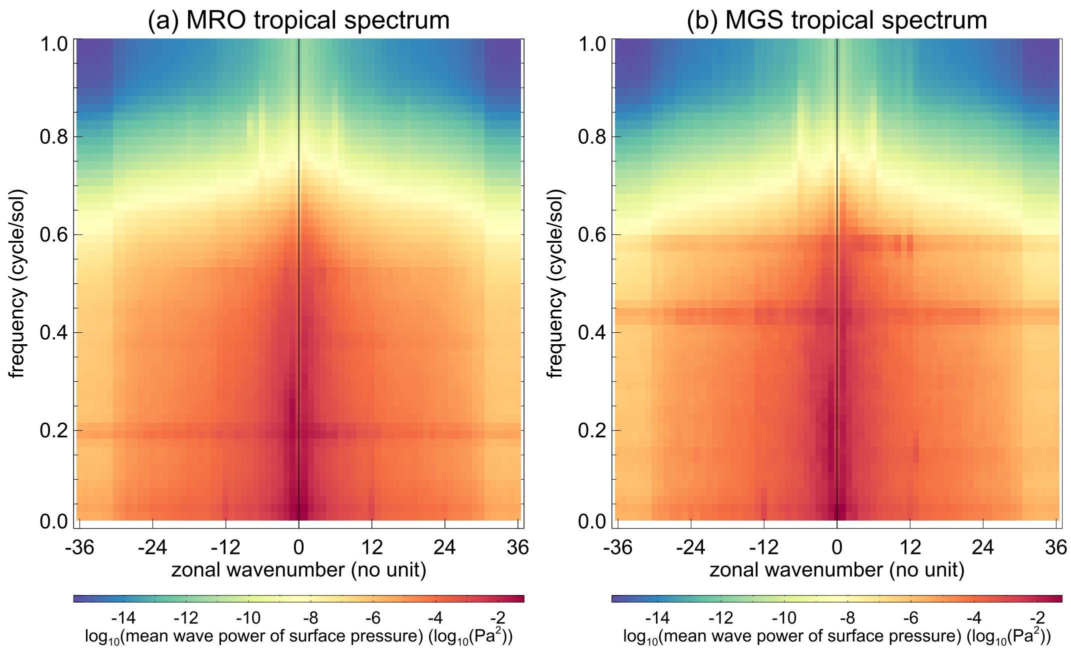

Figure 6. Zonal wavenumber (k) versus time frequency (ω, cycle/sol) $\log_{10}$(mean wave power) spectra derived from OpenMARS (a) Mars Reconnaissance Orbiter years and (b) Mars Global Surveyor years surface pressure Psfc (Pa) for 20°S–20°N during $Ls = 0°–185°$.

"active waves" as those with amplitudes above the mean amplitude plus a threshold, where the threshold is 1σ or 2σ at the corresponding k-ω location.

2.6. Wave Analysis Using OpenMARS

The version 3 OpenMARS reanalysis product (Holmes et al., 2019, 2020) is used as a supplementary data set to examine equatorial waves, where appropriate. The OpenMARS MRO years (MY 28–35) standard database results from an assimilation of the MRO Mars Climate Sounder data into the Open University Mars General Circulation Model. The data set provides continuous 2-hourly global coverage of atmospheric variables, which is convenient for studying atmospheric waves. However, in comparison with terrestrial data assimilation, the Martian observational constraints are sparse. As a result, artificial waves can occasionally occur when data volume/quality changes (Wang, Toigo, & Richardson, 2023), and eddy behaviors can sometimes deviate among different reanalysis products (Battalio, 2022). Furthermore, the spatial resolution of OpenMARS (5° longitude × 5° latitude) is an order of magnitude coarser than typical terrestrial reanalysis products. As a result, equatorial waves with narrow latitudinal structures cannot be resolved well. Therefore, we only use OpenMARS with limited scope.

For analysis of OpenMARS, we first low-pass filtered the 2-hourly time series at each model grid point to remove eddies with wave periods (P) < 1.7 sols using the wavelet method in Wang et al. (2023b). Then, we re-sample the filtered time series at 12-hr intervals and remove the annual cycle by subtracting a low-order polynomial. This step avoids the need to carry large 2-hourly arrays during subsequent computation. We perform wavelet analysis on the resulting signal at each grid point for each MY, separating eddies into different wavelet scales which correspond to different Fourier wave periods. We compose signals for intra-seasonal eddies by summing over the relevant wavelet scales.

We perform 2D FFTs on intra-seasonal eddies using 72 longitudes × 96 sol segments for each model latitude. The mean k-ω spectrum is obtained by averaging the FFT results of all the relevant segments within 20°S–20°N. Figure 6a shows the mean spectrum derived from the $P = 1.7$–60sol surface pressure (Psfc) for the MRO years. Local spectral maxima are seen along $\omega = 0.2$ cycle/sol and $k \sim \pm 12$, as in the MDGM results. In addition, $k = \pm 6$ (half of 12) also seems to be affected at least for $\omega > 0.7$. These suspicious peaks are correlated with the MRO orbit. Their presence in OpenMARS seems likely to result from the observational constraints on the reanalysis,

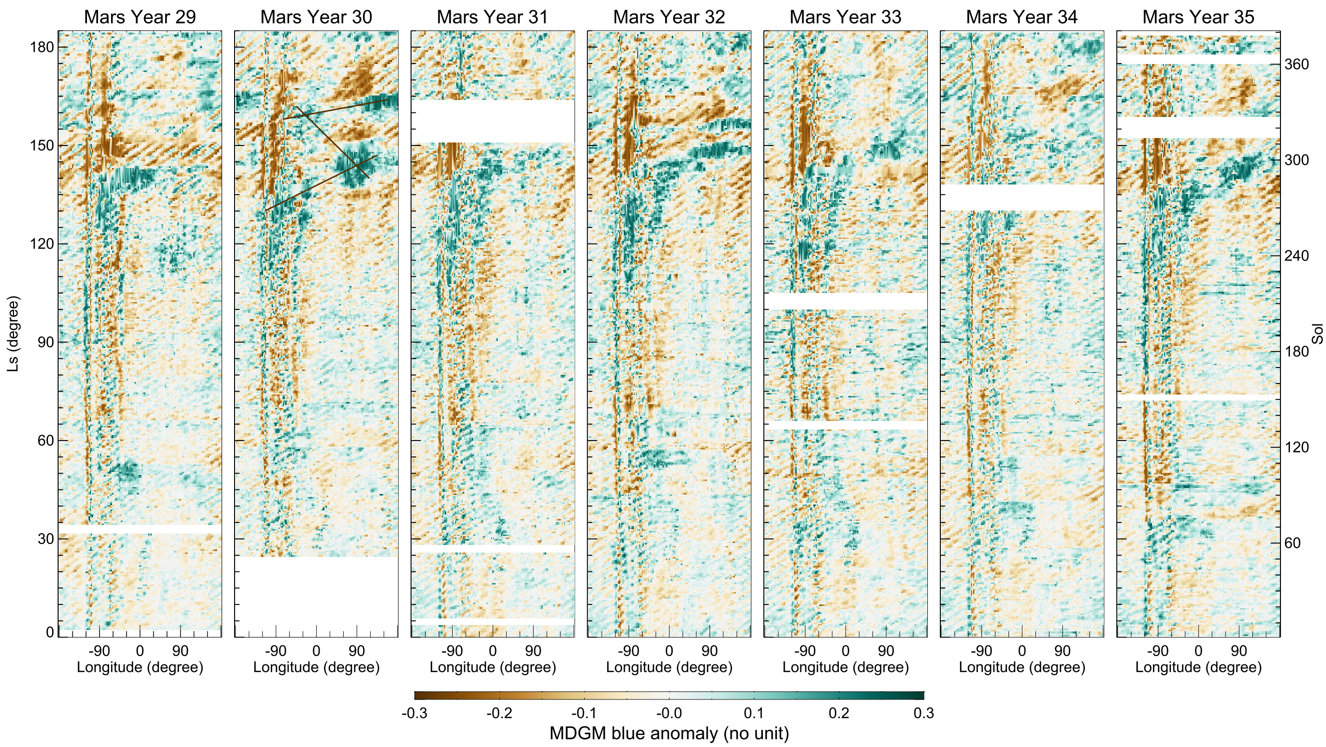

Figure 7. Same as Figure 3c (0.5°S–0°S) but for each Mars year (MY) between MY 29 and 35. Time periods with missing Mars Daily Global Maps are blanked out. Black lines in the MY 30 panel illustrate potential eastward and westward traveling waves of a positive brightness anomaly. Note that there are two full cycles likely in MY32 during $L_S = 135°–160°$. In MY35, between $L_S = 30°$ and 50° (approximately sols 60 to 110), there is also a hint of an oscillation. These are not indicated by lines to avoid figure clutter.

primarily from a single spacecraft on each sol. Similar analysis for the OpenMARS MGS years (MY 24–27) shows that the local maximum k-ω locations (Figure 6b) are different than those for the MRO years, which is consistent with MGS being in a different orbit. The possible spectral contamination in the reanalysis associated with spacecraft orbit is one reason why we only use OpenMARS sparingly in this paper. As we might expect, the k-ω spectra derived for the high latitudes, where the orbit tracks are packed more closely and the diurnal cycle is weaker, appear to be less affected by this issue (Figure S3 in Supporting Information S1).

3. Results

Results are presented first for MDGM (Section 3.1) and then for OpenMARS (Section 3.2). The latter is used to explore potential dynamic connections.

3.1. TCO in MDGMs

This section starts with 7 Mars years of Hovmöller diagrams, which trace the zonal migration of cloud anomalies (Section 3.1.1). The waves contained in these diagrams are then extracted with spectral analysis and the results are compared with theoretical equatorial waves to identify wave types during TCOs (Section 3.1.2). The spectra of the most important waves are used to reconstruct the signals (Section 3.1.3), and the reconstructed signals combined over many latitudes near the equator are used to examine the spatial wave structures (Section 3.1.4).

3.1.1. Hovmöller Diagrams and Seasonality

Figure 7 shows the evolution of the MDGM anomalies for 0.5°S–0°S in Hovmöller diagrams for MY 29–35. The positive and negative anomalies associated with TCOs alternate between the eastern and western hemispheres and they are much more prominent in Triober ($L_s = 135°–185°$) than in Unober and Duober. In MY 30 and 32, there are at least two full cycles of obvious oscillations. In other Mars years, there is at least one.

In MY 29, the TCO starting from $L_s \sim 135°$ is disrupted by a negative anomaly for all longitudes during $L_s = 140°–150°$. This is due to a large dust storm episode in the Argyre-Solis-Valles Marineris (ASV) region, which led to significant atmospheric heating and the disappearance of tropical water ice clouds that year (Battalio & Wang, 2019).

In some Mars years, TCOs may also be present in Unober ($L_s = 0°–70°$) (e.g., MY 35 $L_s = 30°–50°$), but the signal is more muted than that in Triober. In Duober ($L_s = 70°–135°$), when the tropical cloud belt is the most extensive (Smith, 2008; Wolff et al., 2019a), there are no apparent TCOs in MDGMs.

TCOs can be interpreted as interfering eastward and westward traveling waves. Examples of proposed wave propagation are shown using solid lines in the MY 30 panel of Figure 7. As indicated by the slopes of the lines, the inferred waves propagate at different phase speeds. The eastward wave starting near $L_s = 130°$ has a period of $P \sim 20–30$ sols, the westward wave starting near $L_s = 140°$ has a period of $P \sim 40–50$ sols, and the eastward wave starting near $L_s = 155°$ has a period of $P \sim 10–20$ sols. The changes in and the interference of the eastward and westward waves result in the pattern of brightness variation associated with thicker or thinner clouds in the TCO. Note that the wave periods derived in this study emerge from the FFT analysis, and thus the lines in Figure 7 are intended for illustration instead of identification.

3.1.2. Wave Spectrum During TCO

To gain insight into what kinds of tropical waves are active during TCOs, it is useful to examine the wavenumber-frequency (k-ω) dispersion relationships derived from the Hovmöller diagrams and compare them with theoretical equatorial waves. Note that the position and shape of the observed versus idealized analytical solution curves in k-ω space will differ because of the dependence of actual waves upon details of the background winds, thermal structure, and the nature of thermal and mechanical forcing. Thus, the analytical curves should be taken as a guide, not as a definitive solution. The use of these idealized curves to identify wave types is a common practice in terrestrial meteorology (Kiladis et al., 2009; Knippertz et al., 2022; Matsuno, 1966; Wheeler & Kiladis, 1998). Figure 8 shows the spectra of active waves (amplitude >1 or 2σ above the mean; see Section 2.5) for 0.5°S–0°S and the 96-sol segment covering $L_s = 129.8°–180.6°$ of MY 30. The $\log_{10}$(power) of the waves whose amplitudes are above 1σ (Figures 8a) and 2σ (Figure 8b) are colored, and the waves that are below the thresholds or are affected by "ghost" peaks are blanked out.

Consistent with a visual inspection of Figure 7 for MY30, which shows long wavelength, slow traveling waves, most of the power in the space-time spectra (Figure 8ab) is dominated by waves with small wavenumber and low frequency in the purple boxed region, although other waves are also present. Within the high-power clustering around the origin, the TCO cycles observed in MY 30 (Figure 7) are manifested by 3 types of large-scale waves. Specifically, there is strong power at $k = 1$ $\omega = 0.03–0.05$ cycle/sol (eastward $P = 20–33$ sol), $k = 1$ $\omega = 0.08$ cycle/sol (eastward $P = 12.5$ sol), and $k = -1$ $\omega = 0.02–0.03$ cycle/sol (westward $P = 33–50$ sol), consistent with the discussion in Section 3.1.1. The specific k-ω values vary somewhat among the Mars years (Figure S4 in Supporting Information S1), but they are consistently planetary waves with periodicities on the intra-seasonal time scale.

To further highlight the wave behavior in $L_s = 129.8°–180.6°$ of MY 30, we normalize the wave power in Figures 8a and 8b with the mean wave power in Figure 5b. Specifically, if A is the value at a k-ω point from an individual spectrum and B is the value at the same k-ω point from the mean spectrum, then we calculate the power ratio as $r = A/B$. We ignore all suspected ghost peaks and exclude all values when $A < B + 1\sigma$ (Figure 8c) or $A < B + 2\sigma$ (Figure 8d). Figures 8c and 8d show the results for $\log(r)$ when $r > 1.25$ and $r > 1.0$, respectively.

Figure 8cd shows that the three main low wavenumber, low frequency wave modes mentioned before have power ratios $r > 10$ (i.e., $\log10(r) > 1$), illustrating their strong amplification during the TCO time period. The $k = 3$ $\omega = 0.03–0.05$ cycle/sol waves also have large power ratios. They accompany the $k = 1$ $\omega = 0.03–0.05$ cycle/sol waves and may result partly from a modulation by a $k = 2$ stationary wave, which is strong in the Martian atmosphere (Kahre et al., 2020). The stationary wave modulation can also lead to $k = -1$ traveling waves of the same frequencies. Non-linear wave-wave interactions can lead to new waves, which complicates the interpretation and is deferred to future work.

Besides the low frequency large-scale waves, Figure 8 shows that a variety of waves in the k - ω space make statistically significant contributions. To assess what wave types are at play, we compare the classical equatorial

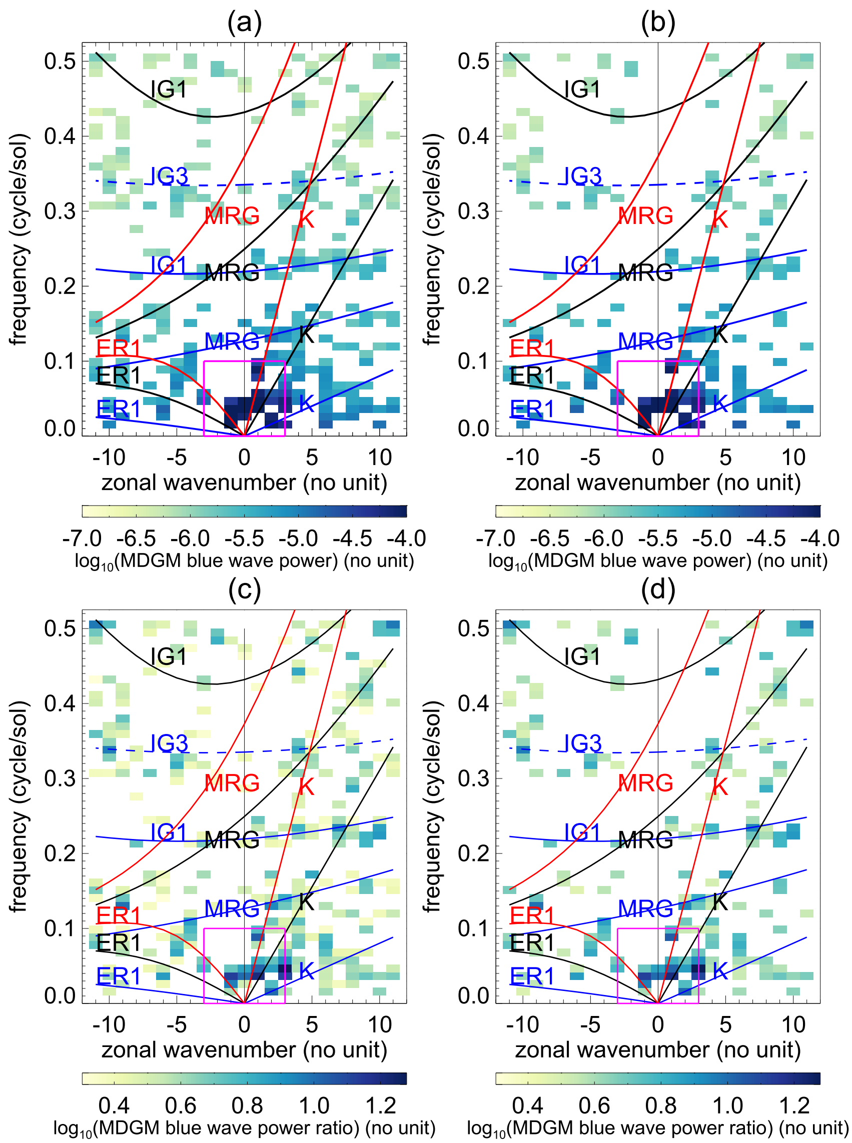

Figure 8. Time frequency (ω, cycle/sol) versus zonal wavenumber (k) spectra derived from Mars Daily Global Maps (MDGMs) for 0.5°S–0°S and Mars Year 30 L_s = 129.8°–180.6°. Colors represent active waves with power above (left column) 1σ and (right column) 2σ of the mean spectrum. The top row shows $\log_{10}$(MDGM blue wave power) and the bottom row shows $\log_{10}$(MDGM blue wave power ratio) (see Section 3.1.2 for definition). The dispersion curves for equatorial shallow water waves (K: Kelvin, MRG: Mixed Rossby Gravity, ERn: Equatorial Rossby mode n, IG: Inertial Gravity mode n, where $n = 1$ or 3) with different equivalent depths (blue: $h_e = 1$ m, black: $h_e = 15$ m, red: $h_e = 75$ m) are overplotted in each panel.

wave theory and overplot the dispersion relationships for shallow water waves in a motionless mean flow on the equatorial β plane (Matsuno, 1966). The theoretical solutions are characterized by equivalent depths (h_e), which relate to wave propagation speeds (Matsuno, 1966; Webster, 2020). As the h_e values are unknown for Martian equatorial waves, nor would they be expected to be constant, we examine several choices. Figure 8 shows the dispersion curves for three equivalent depths, $h_e = 1$ m (blue), 15 m (black), and 75 m (red), and four wave types, eastward propagating Kelvin waves (labeled "K"), westward Equatorial Rossby waves ("ERn"), eastward and westward Inertial Gravity waves ("IGn") and Mixed Rossby-Gravity waves ("MRG"), where n denotes the order of Hermite polynomial for meridional wave structure (Matsuno, 1966).

Different k-ω waves in Figure 8 appear to line up along curves for different wave types depending on the assumed equivalent depths. In reality, the direction and shear of the mean flow are complex (Figure S5 in Supporting

Information S1) and will influence the wavelengths and speeds of equatorial waves (Webster, 2020); hence, the dispersion relationships for waves in the fully non-linear case can deviate from those in the linear wave theory. However, Figure 8 does indicate that the TCO time period likely comprises a rich mixture of different types of waves. Battalio et al. (2022b) showed that waves with periodicities of $P = 1.5$–30 sols were present in the Curiosity and Perseverance surface meteorological variables and exhibited variable phase lags between the sites. The results here suggest that the waves affecting the rovers may be of different types, scales and modes. Notwithstanding the potential wide range of wave types, Figure 8 shows that for the very small wavenumber and low frequency waves dominating the TCO, the equatorial Rossby and Kelvin waves are the major contributors.

3.1.3. Wave Reconstruction for TCO

To investigate how well different waves can explain the observed TCO variability, we reconstruct the Hovmöller diagram from the spectra. Specifically, we perform an inverse FFT using only the active waves above 2σ in different regions of the k-ω space (from Figure 8) for the time-period of interest, and discard all other waves. Figure 9 shows the results for 0.5°S–0°S during $L_s = 135°$–180° of MY 30.

Using all the traveling waves colored in Figure 8b, the reconstructed signal (Figure 9b) resembles the large-scale pattern of the original signal well (Figure 9a). In particular, the positive and negative anomalies associated with the TCO cycles were recovered. Note that the fine-scale wave structure related to the MRO orbit and the signature of the quasi-stationary volcano clouds (near ∼110°W) were manually removed by zeroing their power. The eastward and westward components of the waves in Figure 9b are plotted in Figures 9c and 9d, respectively. Each panel is composed of many k-ω waves traveling in the same direction. The eastward waves appear stronger than the westward waves during this time-period, with the variance of the eastward waves in Figure 9c accounting for ∼72% of that of the reconstructed waves in Figure 9b. The positive anomaly in the eastern hemisphere during $L_s = 130°$–150° (Figure 9b) results from the constructive interference between the eastward and westward waves (Figures 9c and 9d), while the anomaly during $L_s = 160°$–165° appears to be mainly due to the eastward waves (Figure 9c).

We further filter the eastward waves using only those within the k-ω region in Figure 8b that is bordered by the $h_e = 1$ m (blue) and $h_e = 75$ m (red) Kelvin wave dispersion lines. The result (Figure 9e) shows that these Kelvin waves encircle the equator and are responsible for ∼76% of the variance of the eastward waves in Figure 9c. Similarly, we filter the westward waves using only those in Figure 8b that are within the domain covered between the $h_e = 1$ m (blue) and $h_e = 75$ m (red) equatorial Rossby wave dispersion curves. The result (Figure 9f) shows that these waves contribute ∼55% of the variance of the westward propagating waves (Figure 9d).

3.1.4. Wave Structure From MDGMs

We reconstruct the 2D horizonal wave structures of individual waves in the MDGM data using the wave amplitudes and phases for each 0.5° latitude bin within 20°S–20°N. The result in the left column of Figure 10 shows instantaneous snapshots of latitude–longitude structures for several waves with significant amplitudes during $L_s = 135°$–175° of MY 30. For example, the $k = 1$ $P = 32$ sol wave (Row a) and $k = -1$ $P = 48$ sol wave (Row d) are involved in the TCO cycle during $L_s = 130°$–150°, and the $k = 1$ $P = 24$ sol wave (Row b) and $k = 1$ $P = 12$ sol wave (Row c) are involved in the TCO cycle during $L_s = 160°$–165° (Section 3.1.2). We also decompose the reconstructed waves into symmetric and anti-symmetric components with respect to the equator. The symmetric component is given by $y_s(\varphi) = [y(\varphi) + y(-\varphi)]/2$, where φ is latitude and y is the variable of interest and the anti-symmetric component by $y_a(\varphi) = [y(\varphi)\text{-}y(-\varphi)]/2$. The results are shown in the middle and right columns of Figure 10, respectively.

Figure 10 shows a variety of coherent zonal and meridional wave structures. Some have maxima along the equator (e.g., a2, d2), while others are off the equator (e.g., a3, e2); Some are dominated by the symmetric component (e.g., Row a & c), while others have substantial antisymmetric contributions (e.g., Row f); Some show a latitudinal tilt with longitude (e.g., b2), while others appear to roughly align in the meridional direction (e.g., d2, f2). The latitudinal variation of the wave amplitudes (Figure S6 in Supporting Information S1) exhibits different behaviors in terms of the e-folding decay rate with latitude and the number of local peaks. The detailed latitudinal structures with different shapes require models with sufficient resolution to simulate.

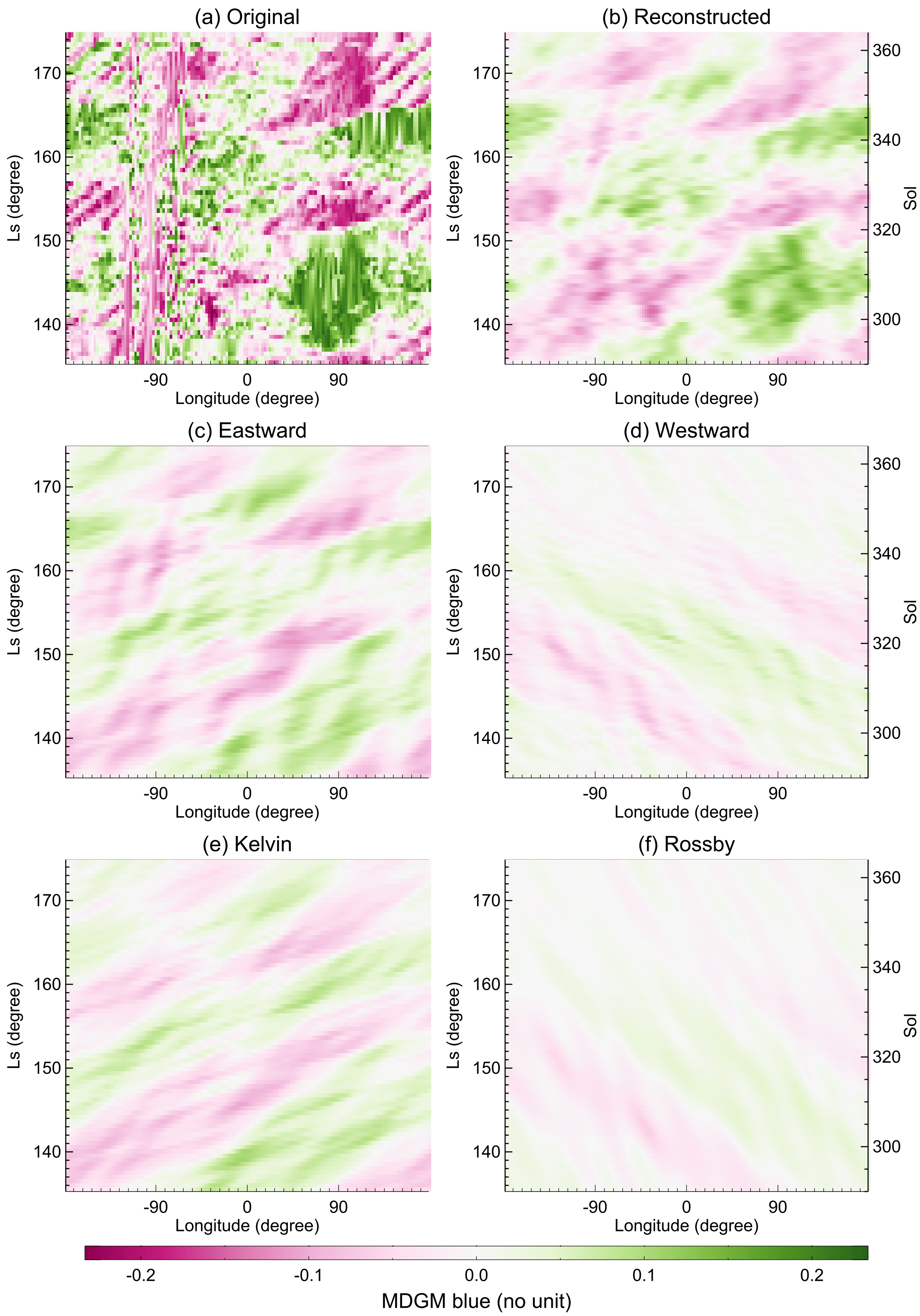

Figure 9. Time (L_s on left axis, sol on right axis) versus longitude Hovmöller diagrams for 0.5°S–0°S during L_s = 135°–180° of Mars Year 30 derived from blue Mars Daily Global Maps (a) before and (b–f) after reconstruction using active waves in different regions of the k–ω spectrum in Figure 8b. The regions used are (b) The whole region, (c) The right ($k > 0$) half corresponding to eastward traveling waves, (d) The left ($k < 0$) half corresponding to westward waves, (e) The region between the blue and red "K" lines on the $k > 0$ side, and (f) The region between the blue and red "ER1" curves on the $k < 0$ side.

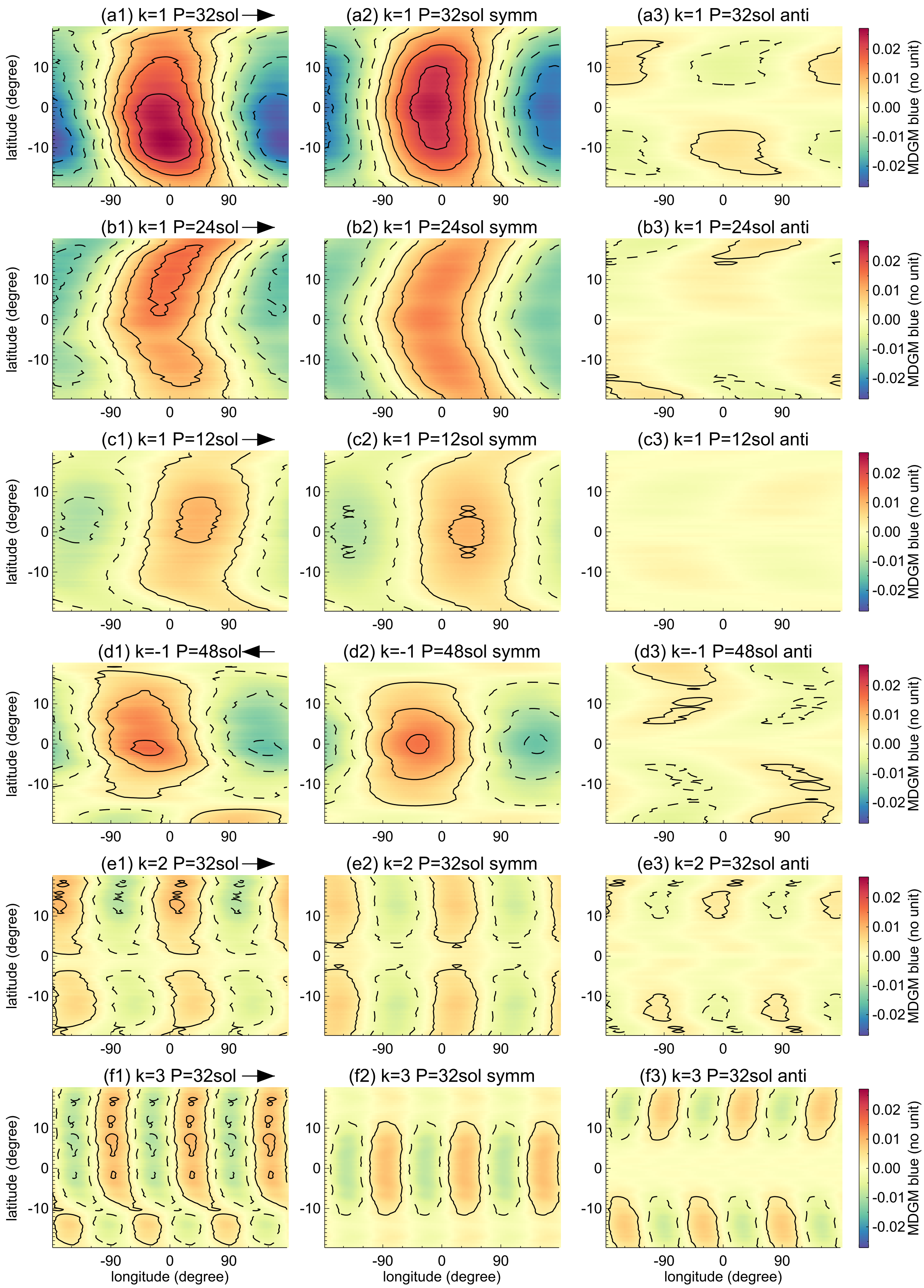

Figure 10. Snapshots of latitude–Longitude structures of waves derived from blue Mars Daily Global Maps during $L_s = 135°–175°$ of Mars Year 30. (Left column) Overall, (middle column) symmetric, (right column) anti-symmetric structures are shown for (Row a) eastward zonal wavenumber $k = 1$, wave period $P = 32$ sol, (Row b) eastward $k = 1$, $P = 24$ sol, (Row c) eastward $k = 1$, $P = 12$ sol, (Row d) westward $k = -1$, $P = 48$ sol, (Row e) eastward $k = 2$, $P = 32$ sol, and (Row f) eastward $k = 3$, $P = 32$ sol. The black arrow above each panel in the left column indicates the wave propagation direction.

As a comparison with MY 30, we examined the structures of the active waves during $L_s = 140°–160°$ of MY 32, which contains a couple of apparent TCO cycles (Figure 7). The variety of wave structures discussed previously are also seen for MY 32 (Figure S7 in Supporting Information S1). Many k-ω waves are active in both MY 32 and MY 30 (Figure 8 and Figure S4 in Supporting Information S1); however, individual wave structures can vary (compare Figure 10 and Figure S7 in Supporting Information S1). For example, the symmetric $k = 1$ $P = 32$ sol wave has its maximum amplitude on the equator in MY 30 (Figure 10a2) but off the equator in MY 32 (Figure S7a2 in Supporting Information S1); The $k = -1$ $P = 48$ sol wave is mostly symmetric in MY 30 (Figure 10d2) but anti-symmetric in MY 32 (Figure S7d3 in Supporting Information S1). The latitudinal structures of shallow water equatorial waves are described by Hermite polynomials of different orders (n), where n determines the symmetry (Matsuno, 1966; Webster, 2020). The differences in wave structure for a k-ω wave between Mars years could be partly due to differences in the composition of the wave modes. Additionally, the differences in atmospheric basic state and non-linear wave interactions may also influence the observed wave structures.

3.2. OpenMARS Analysis

The wave structures derived from MDGM data indicate equatorially trapped waves. This section assesses whether atmospheric variables in data assimilation products support this view. Despite the limitations mentioned in Section 2.6, reanalysis products provide optimally consistent interpretation of limited observations currently available. Hovmöller diagrams and extracted waves are examined in Section 3.2.1 and 3.2.2, respectively.

3.2.1. Intra-Seasonal Eddies in Assimilated Variables

The OpenMARS reanalysis product allows us to examine waves in atmospheric dynamical fields when TCOs are observed in clouds via visual inspection. We concentrate on the $P = 10–40$ sol eddies as they control the large-scale pattern of variability (Figure S8 in Supporting Information S1). Figure 11 shows the OpenMARS Hovmöller diagrams for these eddies at 2.5°N, for temperature T at ∼5 km height and surface pressure Psfc, and for $L_s = 0°–185°$ of MY 30 and MY 35. OpenMARS is affected by a large data gap from late MY 29 to early MY 30 (Holmes et al., 2020) during which the output is essentially unconstrained. Around the time when the data gap ends, strong spurious variations occur as the model tries to adjust toward the data. We thus ignore the results in early Unober of MY 30 (hatched).

Figure 11 shows strong intra-seasonal eddies in Triober, which corresponds to the season with the strongest TCO. The eddies appear to be composed of interfering eastward and westward propagating waves, as indicated by the slopes and widths of the positive and negative anomalies. The phases of the waves vary among the meteorological fields. For example, a negative anomaly in the surface pressure and a positive anomaly in the temperature arrive at 180°E at $L_s = 150°$ in MY 35 (Figures 11c and 11d). Some traveling waves also appear to be present in Unober, at least in the surface pressure of MY 35, which coincides with potential TCOs at the time (Figure 7). However, the Unober eddies and TCOs are not as obvious as those in Triober.

As with the cloud data, the intra-seasonal variability in dynamical fields is clearly suppressed in Duober ($L_s = 70°–135°$). Previous studies found reduced eddy activity within the bottom scale height at high latitudes near solstices, which is referred to as the "solstitial pauses" (Lewis et al., 2016; Toigo & Waugh., 2022). This study shows the suppression of intra-seasonal eddies in the tropics, which extends the characteristics of solstitial pauses. The suppression of tropical intra-seasonal eddies during Duober may be taken as an additional dynamical consequential definition of Duober, as distinct from Unober and Triober. This adds further weight to the sexton pseudo-season definition as a dynamically meaningful way of partitioning the Martian year (Wang, Saidel, et al., 2023).

3.2.2. Wave Structures

To examine the associated eddy structures during the MY 30 Triober TCOs, we extract the eastward and westward $k = 1$ traveling waves of various wave periods from the OpenMARS eddy temperature (dT), eddy zonal wind (du), and eddy meridional wind (dv) for all the vertical model levels, and assemble the results within the tropics in Figure 12.

The theoretical amplitudes of equatorial waves exponentially decay on a length scale of the equatorial radius of deformation (R_e) (Webster, 2020). For an equivalent depth of $h_e = 75$ m (used in Figure 7), R_e (∼445 km) is about 7.5° wide in latitude on Mars, and smaller h_e corresponds to smaller R_e. At the 5° spatial resolution of the

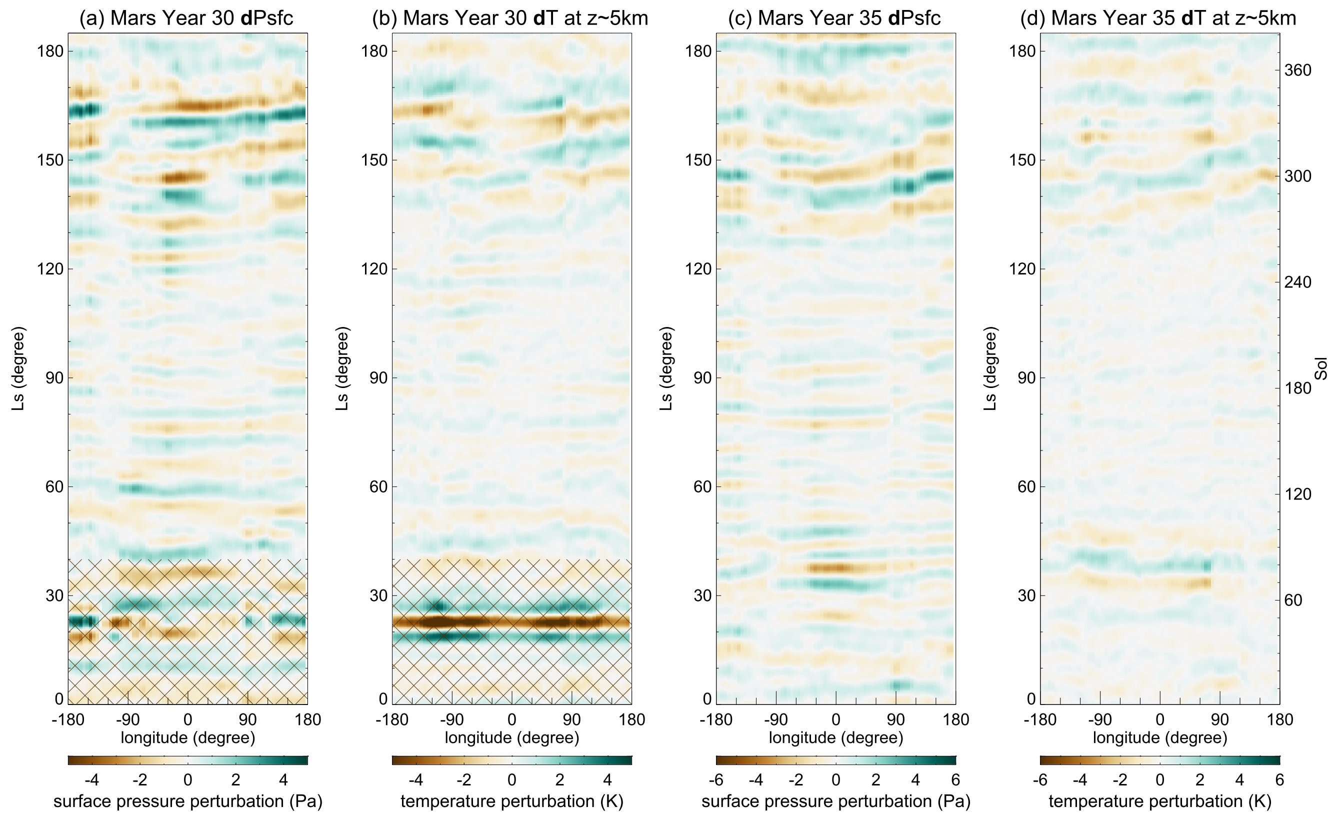

Figure 11. Time versus longitude plots for 2.5°N of wave period $P = 10$–40sol perturbations of (a, c) surface pressure (Psfc) in Pa and (b, d) temperature in K at height z ~5 km for $L_s = 0°$–185° of (a, b) Mars Year (MY) 30 and (c, d) MY 35. Hatches in panels (a, b) indicate ignored time periods (see text). Left axis shows L_s. The right axis in Panel (d) denotes the sol number.

OpenMARS reanalysis, equatorial waves are poorly resolved and possibly aliased among some wave modes and wave types. Nonetheless, OpenMARS is a popular public data set and reasonably captures the general behavior of the TCO in some variables (Figure 11). Thus, we examine wave structures derived from OpenMARS for one time interval and two types of waves.

The top row of Figure 12 shows the horizontal structure of the (a) eastward $k = 1$ $P = 30$ sol and (b) westward $k = -1$ $P = 30$ sol traveling waves at a height of $z \approx 8$ km above the surface at $L_s = 146.3°$ of MY 30, with eddy temperatures as colors and eddy winds as vectors. The corresponding results at $z \approx 16$ km are shown in the second row. The next two rows show the height z versus longitude cross sections of dT and du at 2.5°N at the same moment as that for the upper panels.

As the tropics exhibit weak temperature gradients in comparison with the high latitudes, the temperature anomalies are small, though noticeable wave patterns are still present both horizontally and vertically. dT appears largely symmetric about the equator (Figures 12a–12d) and shows eastward phase shift with height for $z < 16$ km in Figure 12e and westward phase shift with height for $5 < z < 20$ km in Figure 12f. Near the equator, Figures 12a and 12c suggests a tendency of significant du with negligible dv for the eastward wave, which is reminiscent of a Kelvin wave structure (Webster, 2020). However, the pattern is not purely symmetric about the equator and may have been affected by the basic flow or wave aliasing. Substantial wind perturbations are seen beyond 10°N/S in Figures 12a and 12c, which may be related to other equatorial wave types or mid-latitude circulation. The westward wave in Figure 12b shows strong du on the equator, which decays sharply with latitude. It also indicates roughly symmetric gyres about the equator, which is reminiscent of an equatorial Rossby wave. At $z = 16$ km where the background winds are substantial (Figure S5 in Supporting Information S1), off-equatorial cyclonic and anti-cyclonic gyres appear to be phase shifted between the northern and southern hemispheres (Figure 12d). The vertical wavelength of du for the Kelvin type wave (~30 km, Figure 12g) appears longer than that for the Rossby type wave (~15 km, Figure 12h).

10.1029/2024JE008479

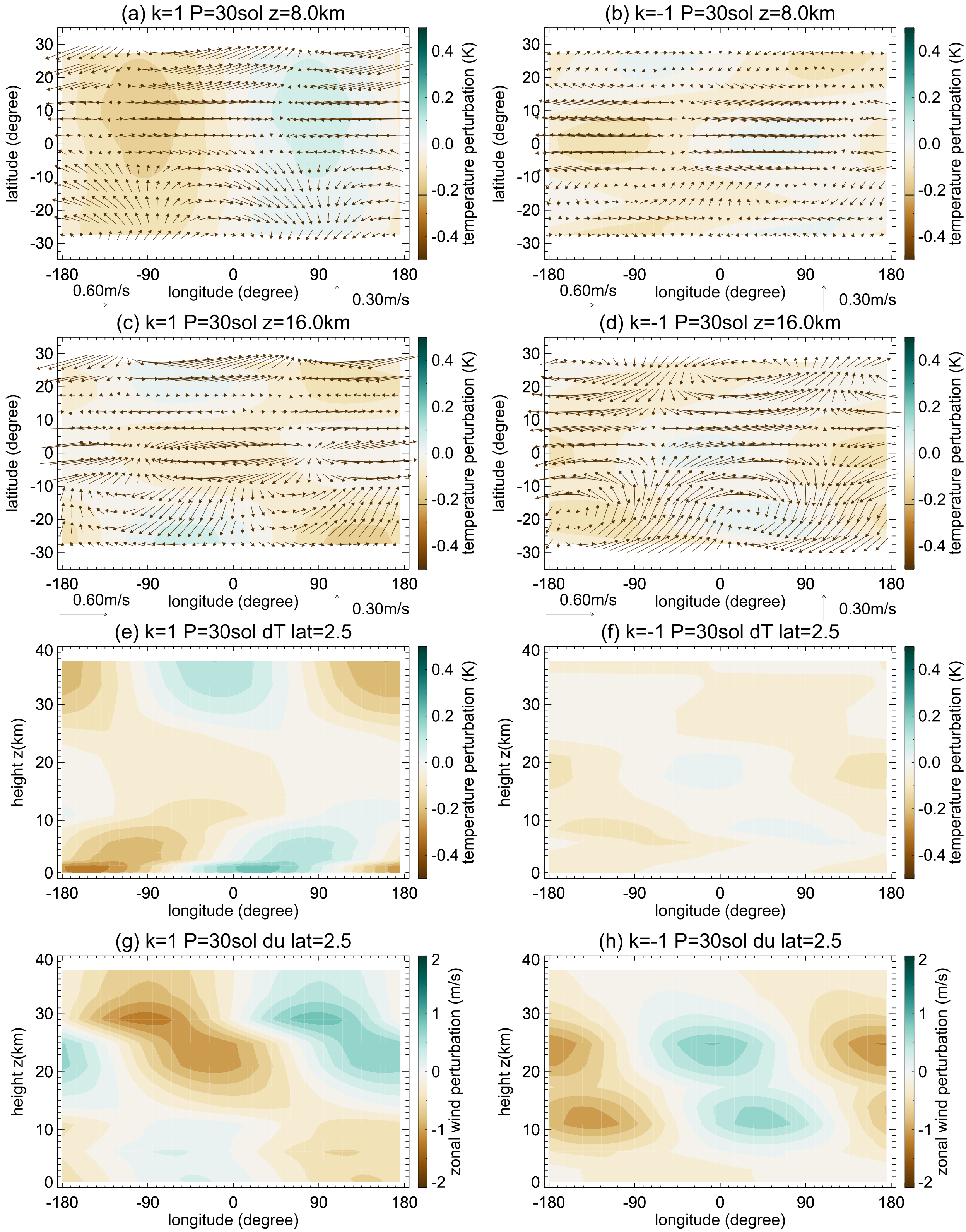

Figure 12. Snapshots of wave structures for (a, c, e, g) eastward traveling zonal wavenumber $k = 1$, wave period $P = 30$ sol and (b, d, f, h) westward traveling $k = -1$, $P = 30$ sol waves derived from OpenMARS during $L_s = 130°–170°$ of Mars Year 30. Perturbation temperature (dT) in K is shown in colors in Panels (a–f) and perturbation zonal wind (du) in m/s is shown in colors in Panels (g, h). Perturbation zonal (du) and meridional (dv) winds (m/s) are overplotted as vectors in Panels (a–d). The latitude–longitude cross sections are for (a, b) $z \sim 8.0$ km and (c, d) $z \sim 16.0$ km. The height (z)–longitude cross sections (e–h) are for 2.5°N.

4. Summary

This paper investigates the Tropical Cloud Oscillation (TCO) in the Martian atmosphere using MDGMs and supplementary datasets (MARCI UV optical depths and OpenMARS reanalysis). The TCO refers to the shift of tropical clouds back and forth between the eastern and western hemispheres on time scales of 10–40 sols. The quasi-regular cyclicality of the TCO could be useful for designing observation strategies for orbiters and rovers. Once the initial pattern of the TCO has been established in a given MY, it may help predict relatively cloudy versus clear time intervals.

TCOs are observed in each MY and are highly characteristic of Triober ($L_s = 135°–185°$). Although the first half of a MY has much fewer and smaller dust storms than the second half in general, Triober dust storms can occasionally reach the equator from the southern mid/high latitudes. These dust storms may provide strong thermal forcing to excite various equatorial waves that provide favorable conditions for the initiation of TCOs.

Space-time spectral analysis was performed to identify waves with different zonal wavenumbers (k) and time frequency (ω). The regular observation pattern of the MRO spacecraft combined with the strong local time variation of the tropical clouds leads to spurious spectrally aliased peaks in all the data analyzed, complicating the interpretation. Consequently, instead of identifying waves from the mean spectrum against a smooth background spectrum, we identify waves with statistically significant amplitudes against the mean spectrum in this study.

A variety of equatorial waves are found during the TCOs. Their k-ω distributions appear to roughly align with the theoretical dispersion relationships of equatorial shallow water waves, including Kelvin waves, Equatorial Rossby waves (ER), Mixed Rossby Gravity waves (MRG), and Inertial Gravity waves (IG) associated with different equivalent depths. Some observed waves may also result from nonlinear wave-wave interactions, such as from modulations of traveling waves by stationary waves.

The general behavior of the TCOs is mainly controlled by a few large-scale traveling waves ($k = 1$) with periodicities on intra-seasonal timescales ($P = 10–40$ sols). The observed horizontal wave structures exhibit a variety of latitudinal shapes with different latitudinal decay rates, indicating different wave modes. The reanalysis results suggest some Kelvin and Rossby wave characteristics with different vertical wavelengths during the TCOs, though the detailed wave structure and behavior requires higher resolution models to resolve.

For a very brief comparison, terrestrial equatorial waves include both dry waves and convectively coupled waves, where the latter have much shallower equivalent depths and slower phase speeds than the former (Webster, 2020). The equivalent depths explored in this paper appear to be closer to those for terrestrial convectively coupled waves than terrestrial dry waves (Wheeler & Kiladis, 1998). The Martian TCO periodicity and characteristics may have some similarities with the terrestrial Madden Julian Oscillation (MJO) (Webster, 2020). However, in the terrestrial atmosphere, latent heat and deep convective clouds play important roles in equatorial wave dynamics and the generation of the MJO, whereas in the Martian atmosphere, latent heat associated with water ice clouds is far less significant than other sources of heating (Richardson et al., 2002).

Data Availability Statement

Mars Daily Global Maps are available at Harvard Dataverse (Wang et al., 2020). The OpenMars database can be downloaded from the Open University (Holmes et al., 2019). MARCI UV ice cloud maps are available at Malin Space Science Systems (Wolff et al., 2019b).

Acknowledgments

This project was supported by NASA MDAP Grant 80NSSC23K1077. Mars Daily Global Maps were supported by NASA Grant 80NSSC20K1056 and were made using the Smithsonian High-Performance Cluster (SI/HPC) at the Smithsonian Institution (https://doi.org/10.25572/SIHPC).

References

Banfield, D., Conrath, B. J., Gierasch, P. J., Wilson, R. J., & Smith, M. D. (2004). Traveling waves in the Martian atmosphere from MGS TES Nadir data. *Icarus*, *170*(2), 365–403. https://doi.org/10.1016/j.icarus.2004.03.015

Barnes, J. R., Haberle, R. M., Wilson, R. J., Lewis, S. R., Murphy, J. R., & Read, P. L. (2017). The global circulation. In *Atmosphere and climate of Mars. Cambridge planetary science series* (pp. 229–294).

Battalio, J. M. (2022). Transient eddy energetics on Mars in three reanalysis datasets. *Journal of the Atmospheric Sciences*, *79*(2), 361–382. https://doi.org/10.1175/JAS-D-21-0038.1

Battalio, J. M., Martinez, G., Newman, C., de la Torre Juarez, M., Sanchez-Lavega, A., & Viudez-Moreiras, D. (2022). Planetary waves traveling between mars science Laboratory and Mars 2020. *Geophysical Research Letters*, *49*, 21. https://doi.org/10.1029/2022GL100866

Battalio, M., & Wang, H. (2019). The Aonia-Solis-Valles dust storm track in the southern hemisphere of Mars. *Icarus*, *321*, 367–378. https://doi.org/10.1016/j.icarus.2018.10.026

Bell, J. F. I. I. I., Wolff, M. J., Malin, M. C., Calvin, W. M., Cantor, B. A., Caplinger, M. A., et al. (2009). Mars Reconnaissance Orbiter Mars Color Imager (MARCI): Instrument description, calibration, and performance. *Journal of Geophysical Research*, *114*(E8), E08S92. https://doi.org/10.1029/2008JE003315

Benson, J. L., Bonev, B. P., James, P. B., Shan, K. J., Cantor, B. A., & Caplinger, M. A. (2003). The seasonal behavior of water ice clouds in the Tharsis and Valles Marineris regions of Mars: Mars orbiter camera observations. *Icarus*, *165*(1), 34–52. https://doi.org/10.1016/S0019-1035(03)00175-1

Bradski, G. (2000). The OpenCV library. *Dr. Dobb's Journal of Software Tools*, *120*, 122–125.

Clancy, R. T., Grossman, A. W., Wolff, M. J., James, P. B., Rudy, D. J., Billawala, Y. N., et al. (1996). Water vapor saturation at low altitudes around Mars aphelion: A key to Mars climate? *Icarus*, *122*(1), 36–62. https://doi.org/10.1006/icar.1996.0108

Clancy, R. T., Montmessin, F., Benson, J., Daerden, F., Colaprete, A., & Wolff, M. J. (2017). Mars clouds. In *The atmosphere and climate of Mars* (pp. 42–75). Chapter 5. https://doi.org/10.1017/9781139060172.005

Giuranna, M., Wolkenberg, P., Grassi, D., Aronica, A., Aoki, S., Scaccabarozzi, D., et al. (2021). The current weather and climate of Mars: 12 years of atmospheric monitoring by the Planetary Fourier Spectrometer on Mars Express. *Icarus*, *353*, 113406. https://doi.org/10.1016/j.icarus.2019.113406

Guha, B. K., Panda, J., & Wu, Z. (2021). Observation of aphelion cloud belt over Martian tropics, its evolution, and associated dust distribution from MCS data. *Advances in Space Research*, *67*(4), 1392–1411. https://doi.org/10.1016/j.asr.2020.11.010

Hinson, D. P., & Wilson, R. J. (2023). Dust-storm forcing of Rossby waves on Mars. *Icarus*, *412*, 115998. https://doi.org/10.1016/j.icarus.2024.115998

Holmes, J. A., Lewis, S. R., & Patel, M. R. (2019). OpenMARS database [Dataset]. The Open University Collection. https://doi.org/10.21954/ou.rd.c.4278950

Holmes, J. A., Lewis, S. R., & Patel, M. R. (2020). OpenMARS: A global record of Martian weather from 1999 to 2015. *Planetary and Space Science*, *188*, 104962. https://doi.org/10.1016/j.pss.2020.104962

Hovmöller, E. (1949). The trough-and-ridge diagram. *Tellus*, *1*(2), p62–66. https://doi.org/10.1111/j.2153-3490.1949.tb01260.x

Kahre, M. A., Haberle, R. M., Hollingsworth, J. L., & Wolff, M. J. (2020). MARCI-observed clouds in the Hellas basin during northern hemisphere summer on Mars: Interpretation with the NASA/Ames legacy Mars global climate model. *Icarus*, *338*, 113512. https://doi.org/10.1016/j.icarus.2019.113512

Kahre, M. A., Haberle, R. M., Wilson, R. J., Urata, R. A., Steakley, K. E., Brecht, A. S., et al. (2023). The NASA Ames legacy Mars global climate model: Radiation code error correction and new baseline water cycle simulation. *Icarus*, *400*, 115561. https://doi.org/10.1016/j.icarus.2023.115561

Kiladis, G. N., Wheeler, M., Haertel, P. T., Straub, K. H., & Roundy, P. E. (2009). Convectively coupled equatorial waves. *Reviews of Geophysics*, *47*(2), RG2003–2009. Paper number 2008RG000266. https://doi.org/10.1029/2008rg000266

Knippertz, P., Gehne, M., Kiladis, G. N., Kikuchi, K., Rasheeda Satheesh, A., Roundy, P. E., et al. (2022). The intricacies of identifying equatorial waves. *Quarterly Journal of the Royal Meteorological Society*, *148*(747), 2814–2852. https://doi.org/10.1002/qj.4338

Lemmon, M. T., Wolff, M. J., Smith, M. D., Clancy, R. T., Banfield, D., Landis, G. A., et al. (2004). Atmospheric imaging results from the Mars exploration rovers: Spirit and Opportunity. *Science*, *306*(5702), 1753–1756. https://doi.org/10.1126/science.1104474

Lewis, S. R., Mulholland, D. P., Read, P. L., Montabone, L., Wilson, R. J., & Smith, M. D. (2016). The solsticial pause on Mars: 1. A planetary wave reanalysis. *Icarus*, *264*, 456–464. https://doi.org/10.1016/j.icarus.2015.08.039

Matsuno, T. (1966). Quasi-Geostrophic motions in the equatorial area. *Journal of the Meteorological Society of Japan*, *44*(1), 25–43. https://doi.org/10.2151/jmsj1965.44.1_25

Richardson, M. I., Wilson, R. J., & Rodin, A. V. (2002). Water ice clouds in the Martian atmosphere: General circulation model experiments with a simple cloud scheme. *Journal of Geophysical Research*, *107*(E9), 5064. https://doi.org/10.1029/2001JE001804

Smith, B. A. (1961). Blue clearing during the 1960-61 mars apparition. *Publications of the Astronomical Society of the Pacific*, *73*, 456–459. https://doi.org/10.1086/127730

Smith, M. D. (2008). Spacecraft observations of the Martian atmosphere. *Annual Review of Earth and Planetary Sciences*, *36*(1), 191–219. https://doi.org/10.1146/annurev.earth.36.031207.124334

Smith, M. D. (2019). Local time variation of water ice clouds on Mars as observed by THEMIS. *Icarus*, *333*, 273–282. https://doi.org/10.1016/j.icarus.2019.06.009

Steele, L. J., Lewis, S. R., & Patel, M. R. (2014). The radiative impact of ice cloud from a reanalysis of Mars Climate Sounder data. *Geophysical Research Letters*, *41*(13), 4471–4478. https://doi.org/10.1002/2014GL060235

Toigo, A. D., & Waugh, D. W. (2022). Connections between the transient polar warming and solstitial pause on Mars. *The Planetary Science Journal*, *3*(9), 208. https://doi.org/10.3847/PSJ/ac8550

Wang, H., Battalio, J. M., & Huber, Z. (2020). MRO MARCI Mars daily global maps V2 [dataset]. *Harvard Dataverse*, V4. https://doi.org/10.7910/DVN/U3766S

Wang, H., & Gonzalez Abad, G. (2021). Cloud masks derived from the Mars daily global maps and an application to the tropical cloud belt on Mars. *Geosciences*, *11*(8), 325. https://doi.org/10.3390/geosciences11080324

Wang, H., & Ingersoll, A. P. (2002). Martian clouds observed by Mars Global Surveyor Mars Orbiter Camera. *Journal of Geophysical Research*, *108*(E9), 5110. https://doi.org/10.1029/2001JE001815

Wang, H., Saidel, M., Richardson, M. I., Toigo, A. D., & Battalio, J. M. (2023). Martian dust storm distribution and annual cycle from Mars daily global map observations. *Icarus*, *394*, 115416. https://doi.org/10.1016/j.icarus.2022.115416

Wang, H., Toigo, A. D., & Richardson, M. I. (2023). Simulated atmospheric response to large-scale dust forcing and implications for Martian dust storm growth. *Journal of Geophysical Research*, *128*(10), e2023JE007956. https://doi.org/10.1029/2023JE007956

Webster, P. J. (2020). *Dynamics of the tropical atmosphere and oceans. Series: Advancing weather and climate science*. John Wiley-Blackwell. ISBN-13 978-0470662564.

Wheeler, M., & Kiladis, G. N. (1998). Convectively coupled equatorial waves: Analysis of clouds and temperature in the wavenumber-frequency domain. *Journal of the Atmospheric Sciences*, *56*(3), 374–399. https://doi.org/10.1175/1520-0469(1999)056<0374:ccewao>2.0.co;2

Willame, Y., Vandaele, A. C., Depiesse, C., Lefevre, F., Letocart, V., Gillotay, D., & Montmessin, F. (2017). Retrieving cloud, dust and ozone abundances in the Martian atmosphere using SPICAM/UV nadir spectra. *Planetary and Space Science*, *142*, 9–25. https://doi.org/10.1016/j.pss.2017.04.011

Wilson, R. J., & Guzewich, S. D. (2014). Influence of water ice clouds on nighttime tropical temperature structure as seen by the Mars Climate Sounder. *Geophysical Research Letters*, *41*(10), 3375–3381. https://doi.org/10.1002/2014GL060086

Wolff, M. J., Clancy, R. T., Kahre, M. A., Haberle, R. M., Forget, F., Cantor, B. A., & Malin, M. C. (2019a). Mapping water ice clouds on Mars with MRO/MARCI. *Icarus*, *332*, 24–49. https://doi.org/10.1016/j.icarus.2019.05.041

Wolff, M. J., Clancy, R. T., Kahre, M. A., Haberle, R. M., Forget, F., Cantor, B. A., & Malin, M. C. (2019b). MRO MARCI ice cloud optical depth products [Dataset]. *Malin Space Science Systems*. https://www.msss.com/mro_marci_iceclouds

Wolff, M. J., Fernando, A., Smith, M. D., Forget, F., Millour, E., Atwood, S. A., et al. (2022). Diurnal variations in the Aphelion cloud belt as observed by the Emirates Exploration Imager (EXI). *Geophysical Research Letters*, *49*, 18. https://doi.org/10.1029/2022GL100477

Wu, D. L., Hays, P. B. m., & Skinner, W. R. (1995). A least-squares method for spectral analysis of space-time series. *Journal of the Atmospheric Sciences*, *52*(20), 3501–3511. https://doi.org/10.1175/1520-0469(1995)052<3501:ALSMFS>2.0.CO;2

Zurek, R. W., & Smrekar, S. E. (2007). An overview of the Mars Reconnaissance Orbiter (MRO) science mission. *Journal of Geophysical Research*, *112*(E5), E05S01. https://doi.org/10.1029/2006JE002701

Supporting material for

Large scale oscillations in the Martian tropical cloud belt

Huiqun Wang[1], Mark I. Richardson[2], Anthony D. Toigo[3], Claire E. Newman[2]

[1] Center for Astrophysics | Harvard-Smithsonian, Cambridge, MA, USA.
[2] Aeolis Research, Chandler, AZ, USA.
[3] John Hopkins University Applied Physics Laboratory, Laurel, MD, USA.

Contents of this file

Figures S1 to S8

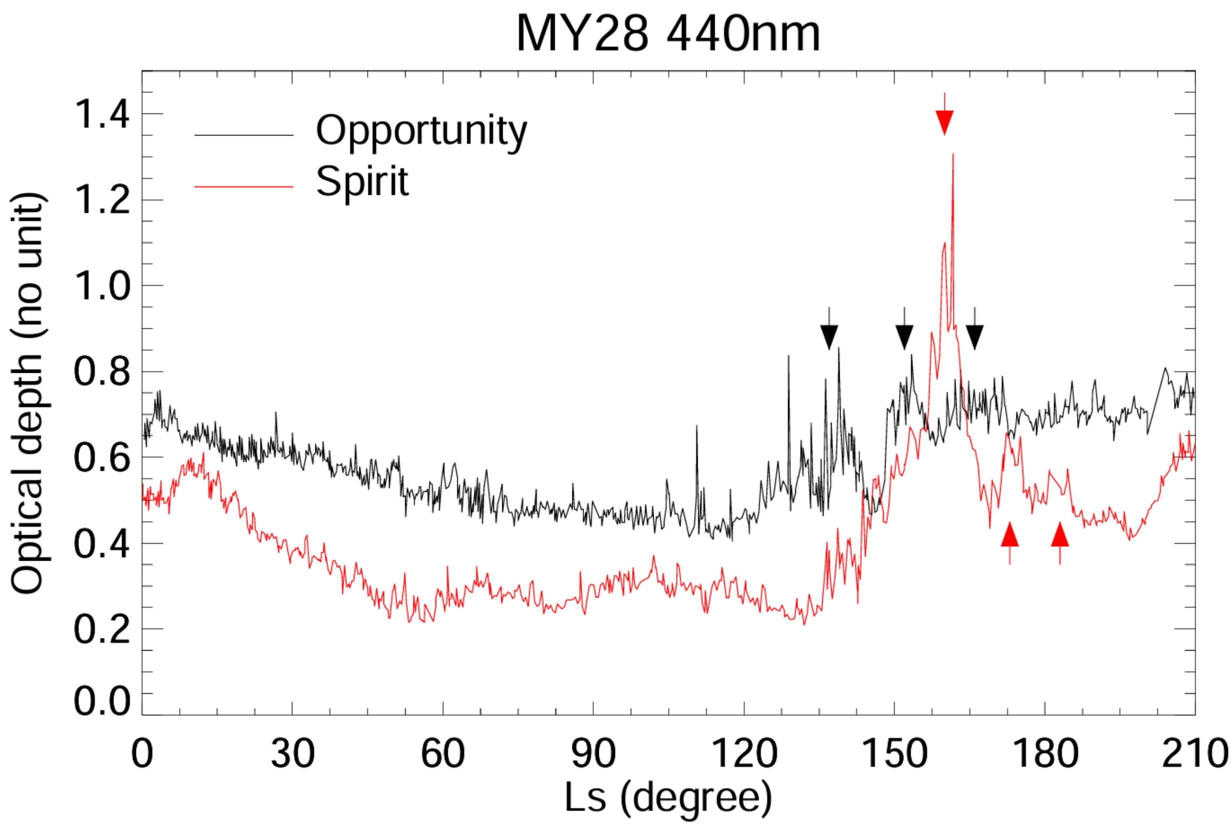

Figure S1. Optical depth (unitless) at 440nm observed by (black) Opportunity and (red) Spirit Mars Exploration Rover (MER) as a function of L_s for Mars Year (MY) 28. Arrows indicate local peaks in late northern summer. The peaks suggest the presence of an alternation of clouds between the locations of the rovers in late northern summer.

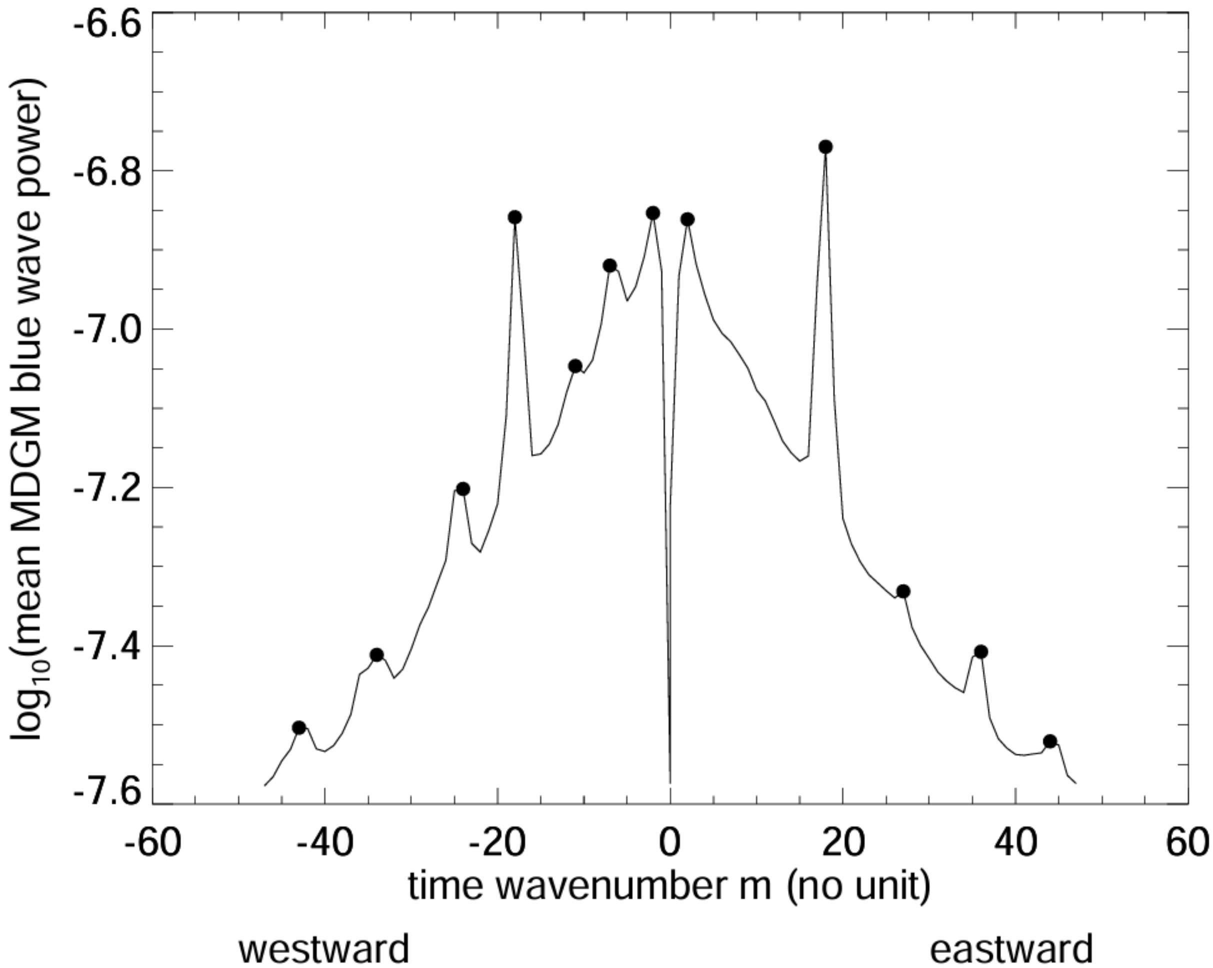

Figure S2. Log_{10} of the average wave power for all zonal wavenumbers (k) of the eastward and westward traveling waves in the mean spectrum (Fig. 5b) as a function of the time wavenumber (m). m=$\pm$1corresponds to a wave period P = 96 sols, m = $\pm$2 corresponds to P = 48 sols, and so on. Eastward waves are plotted on the right half plane (m > 0) and westward waves on the left half plane (m < 0). Suspected ghost peaks are indicated by dots.

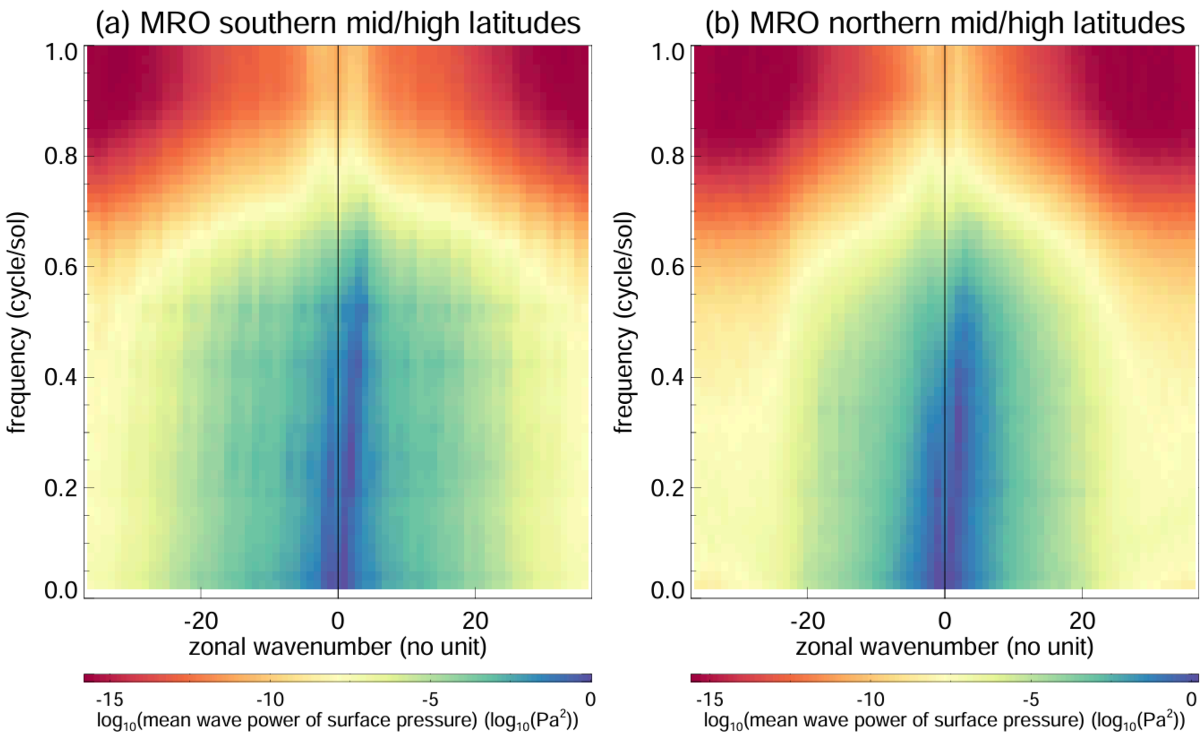

Figure S3. Zonal wavenumber (k, unitless) versus time frequency (ω, cycle/sol) plot of Log_{10}(mean wave power) derived from OpenMARS surface pressure (Pa) for (a) 75°S-45°S and (b) 45°N-75°N during Ls = 0° - 185° of MY 28 – 35 which are the MRO years.

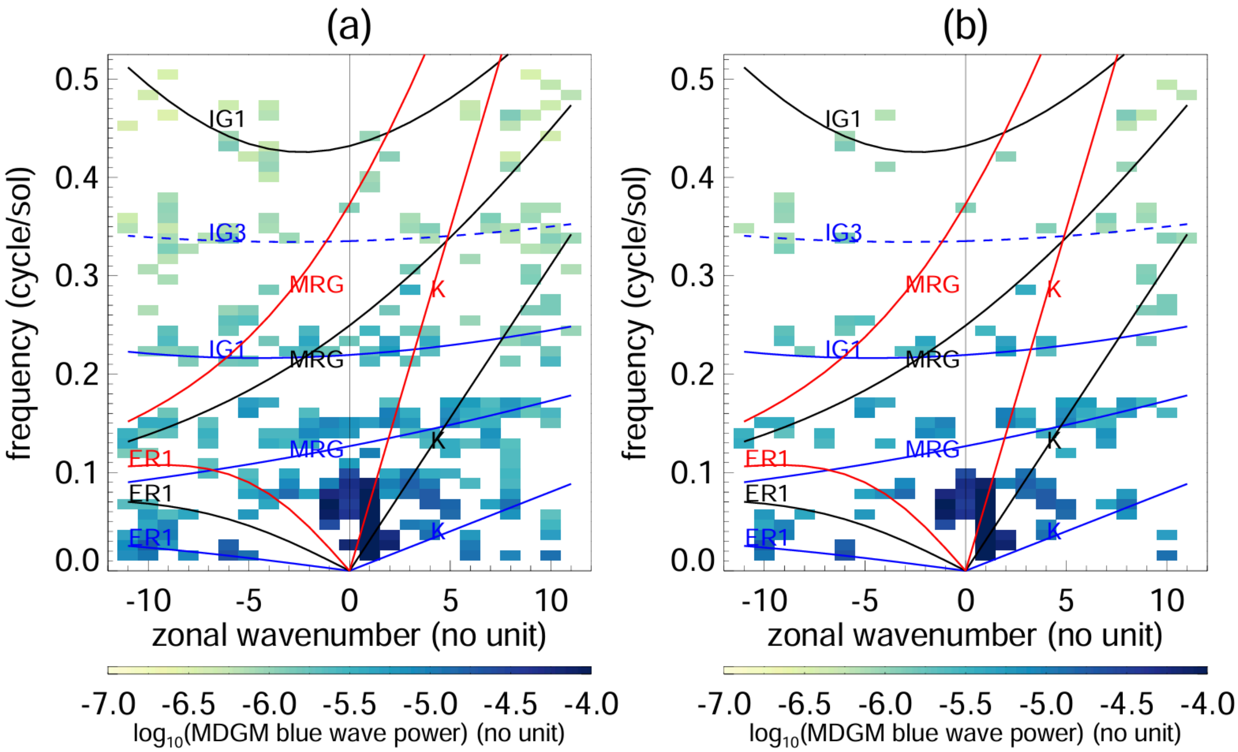

Figure S4. Zonal wavenumber (k, unitless) versus time frequency (ω, cycle/sol) $\log_{10}$(wave power) spectra derived from blue MDGMs for 0.0°N – 0.5°N and Mars Year 32 L_s = 126° – 176°. Colors represent active waves with wave power above (a) 1σ and (b) 2σ of the mean wave power spectrum. The dispersion curves for equatorial shallow water waves (K: Kelvin, MRG: Mixed Rossby Gravity, ERn: Equatorial Rossby mode n, IGn: Inertial Gravity mode n, where n = 1 or 3) with different equivalent depths h_e (blue: h_e = 1 m, black: h_e = 15 m, red: h_e = 75 m) are overplotted in each panel.

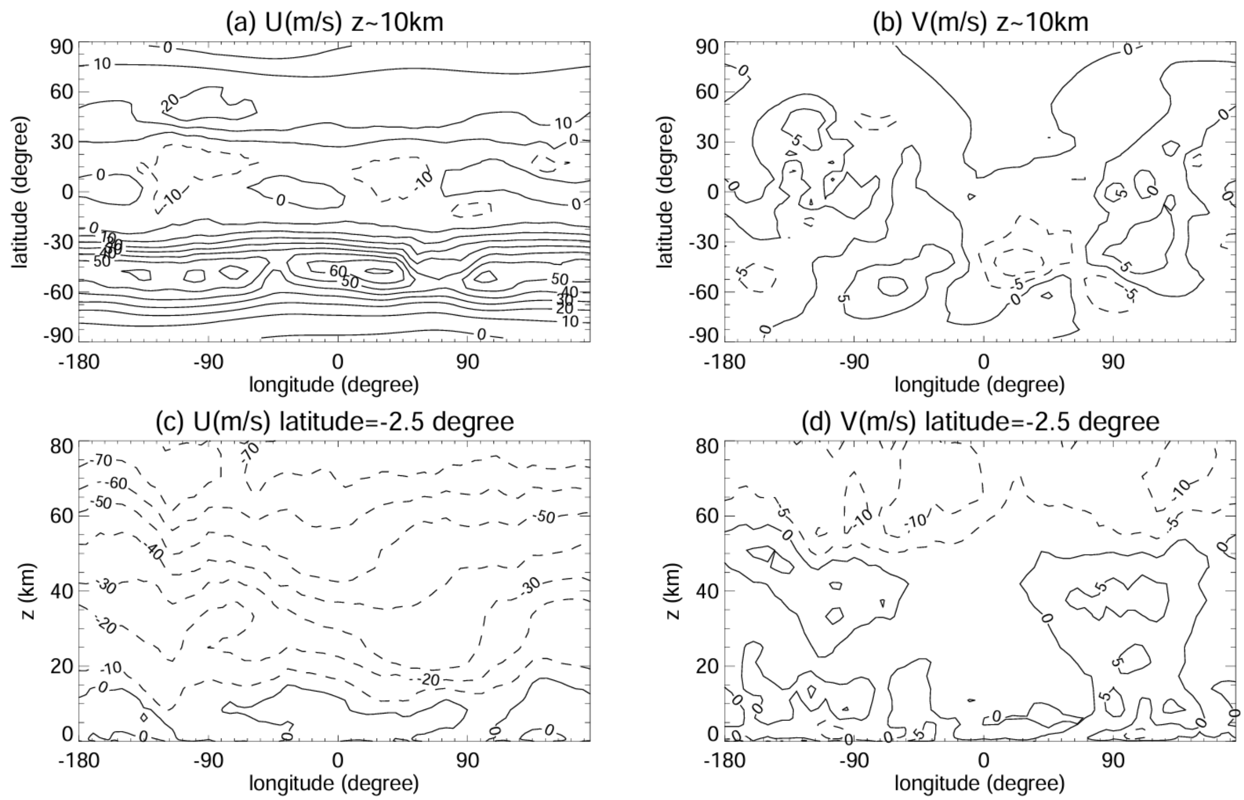

Figure S5. OpenMARS 60-sol mean (a, c) zonal wind (U, m/s) and meridional wind (V, m/s) centered at L_s = 150° of Mars Year 30. (a, b) latitude – longitude cross section at z ~10km. (c, d) height (z) – longitude cross section at 2.5°S.

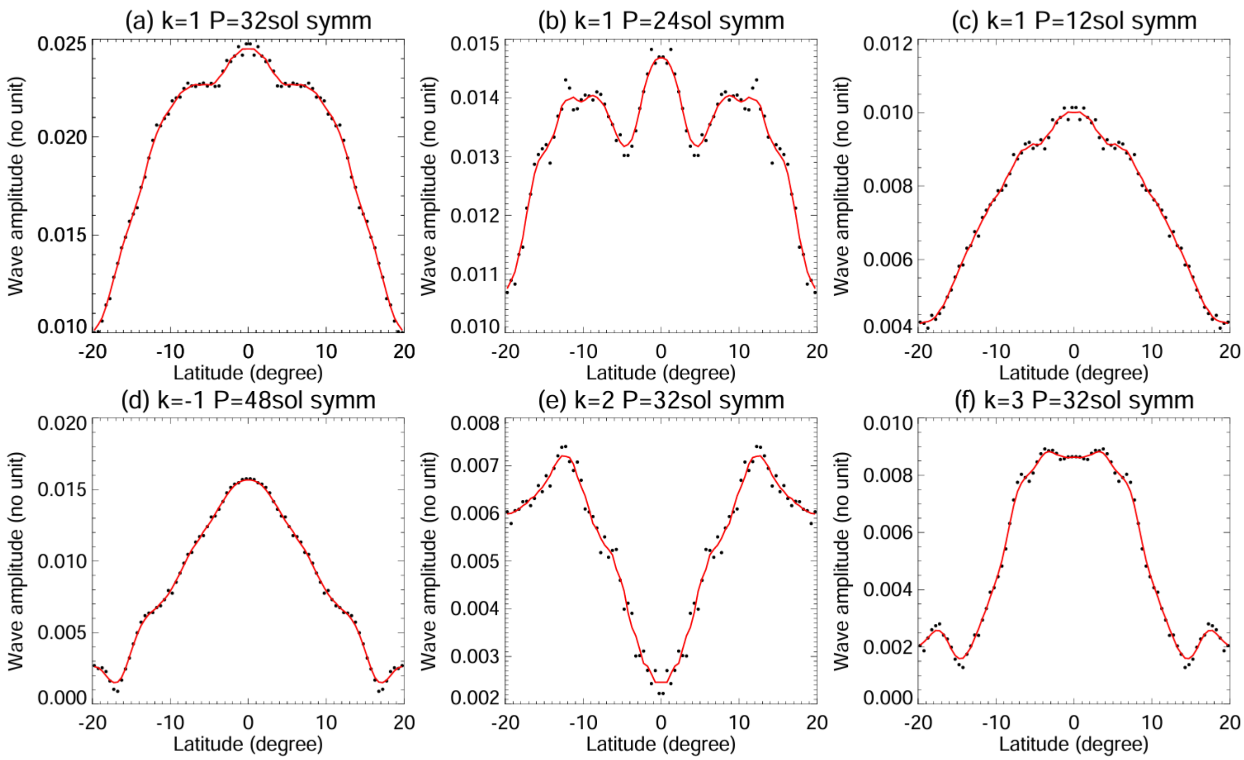

Figure S6. Unitless wave amplitude (*i.e.*, absolute value) as a function of latitude derived from blue MDGMs during L_s = 135° – 175° of Mars Year 30 for (a) eastward zonal wavenumber k = 1, wave period P = 32sol symmetric wave, (b) eastward k=1, P = 24sol symmetric wave, (c) eastward k = 1, P = 12sol symmetric wave, (d) westward k = -1, P = 48sol symmetric wave, (e) eastward k = 2, P = 32sol symmetric wave, and (f) eastward k = 3, P = 32sol symmetric wave. Data for each latitude bin are plotted with black dots. Red lines are the 5-point smoothed curves.

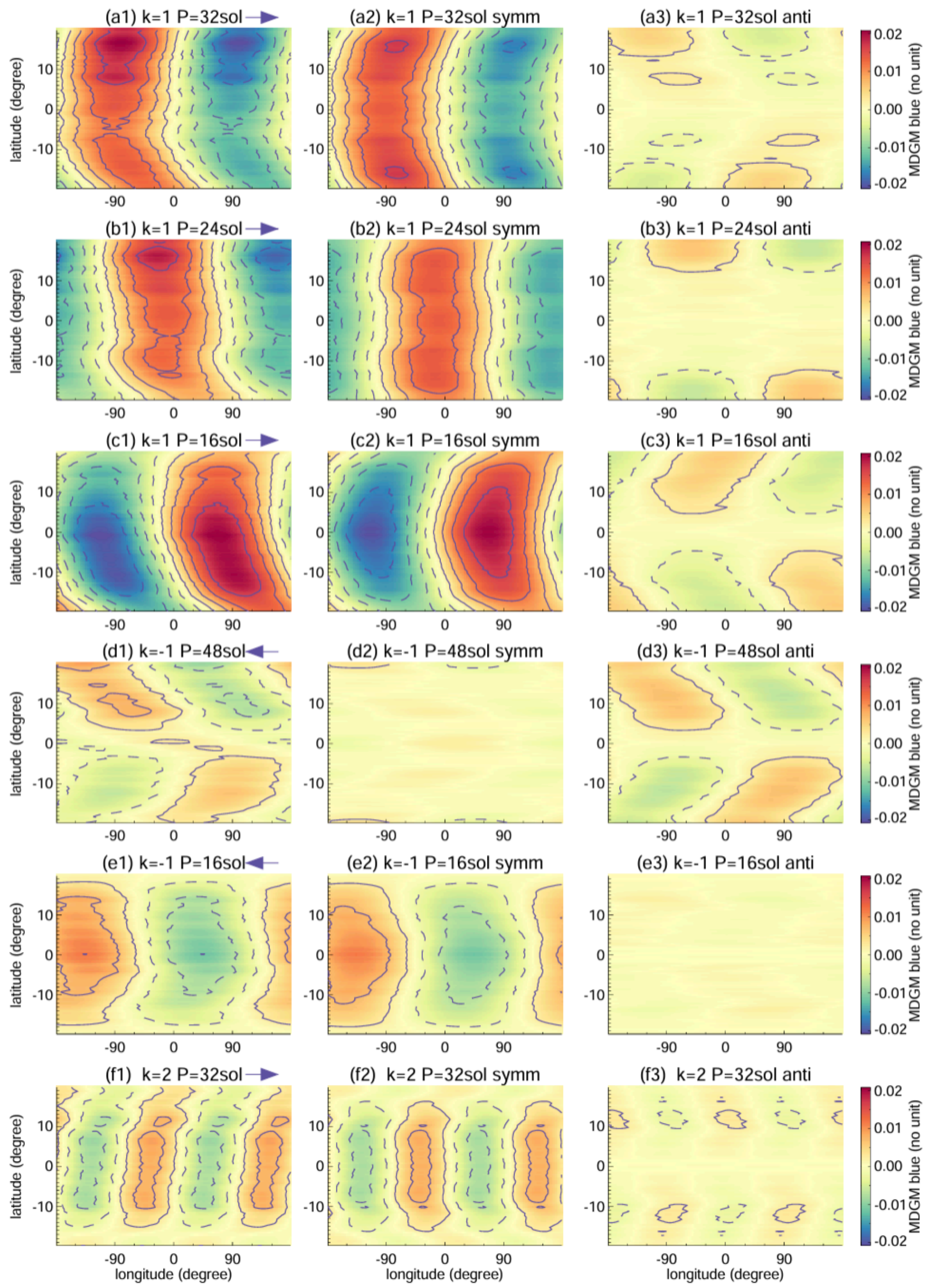

Figure S7. Snapshots of latitude – Longitude structures of waves (unitless) derived from blue MDGMs during $L_s = 126° – 176°$ of Mars Year 32. (left column) Overall, (middle column) symmetric, (right column) anti-symmetric structures are shown for (Row a) eastward zonal wavenumber k = 1, wave period P = 32 sol, (Row b) eastward k = 1, P = 24 sol, (Row c) eastward k = 1, P = 16sol, (d) westward k = -1, P = 48 sol, (Row e) westward k = -1, P = 16 sol, and (Row f) eastward k = 2, P = 32 sol. Black arrow above each panel in the left column indicates the direction of wave propagation.

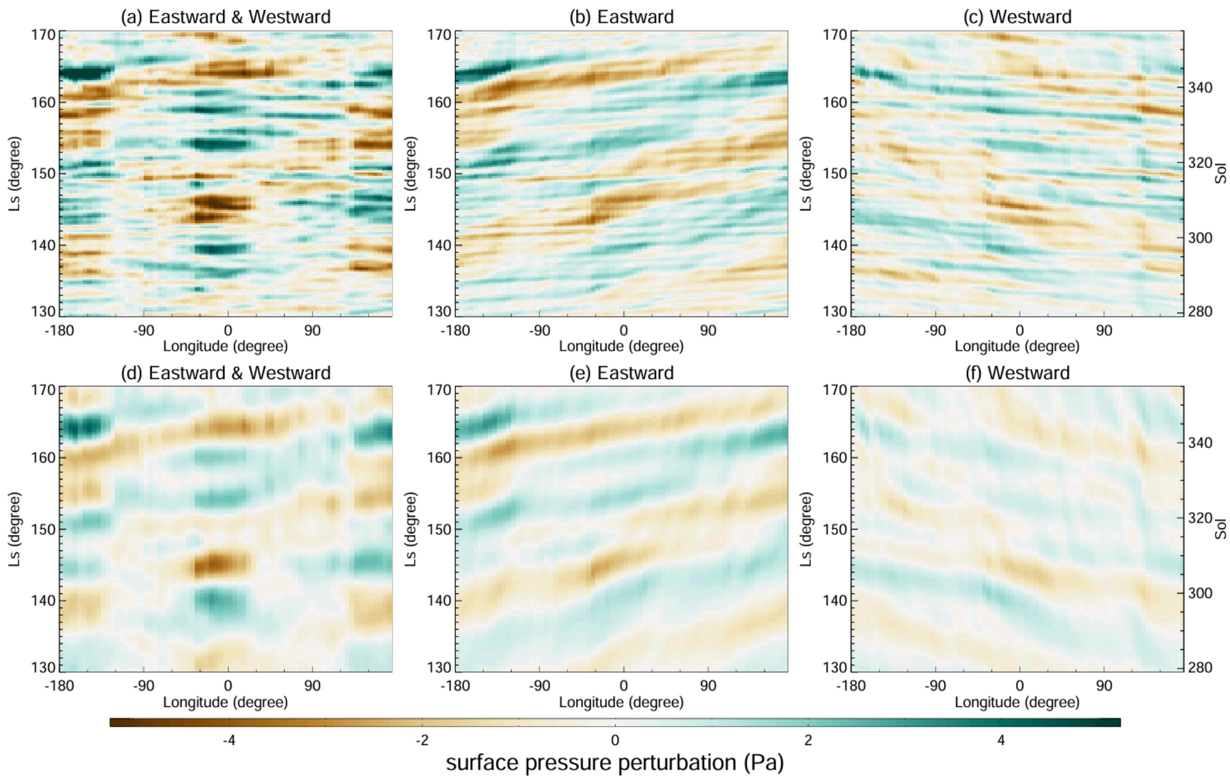

Figure S8. Time versus longitude plots of traveling waves in OpenMARS surface pressure Psfc (Pa) at 2.5°S during Mars Year 30 L_s = 130°-170° when apparent Tropical Cloud Oscillations (TCOs) are observed. Solar longitude L_s is shown on the left axis. Sol number is shown on the right axis. Time increases upward. Top row shows (a) wave period P = 1.7 – 60.0sol eddies and their (b) eastward and (c) westward components. Bottom row shows (d) P = 10.0 – 40.0sol eddies and their (e) eastward and (f) westward components. The P = 10.0 – 40.0sol eddies clearly control the large-scale pattern of variability.